

# Charge-carrier dynamics and regulation strategies in perovskite light-emitting diodes: From materials to devices

Cite as: Appl. Phys. Rev. **9**, 021308 (2022); doi: [10.1063/5.0080087](https://doi.org/10.1063/5.0080087)

Submitted: 29 November 2021 · Accepted: 11 April 2022 ·

Published Online: 13 May 2022



[View Online](#)



[Export Citation](#)



[CrossMark](#)

Lili Xu, Gaoyu Liu, Hengyang Xiang,<sup>a)</sup> Run Wang, Qingsong Shan, Shichen Yuan, Bo Cai, <sup>a)</sup> Zhi Li, <sup>a)</sup> Weijin Li, Shengli Zhang, <sup>a)</sup> and Haibo Zeng<sup>a)</sup>

## AFFILIATIONS

MIIT Key Laboratory of Advanced Display Materials and Devices, School of Materials Science and Engineering, Nanjing University of Science and Technology, Nanjing 210094, China

<sup>a)</sup>Authors to whom correspondence should be addressed: [xiang.hengyang@njust.edu.cn](mailto:xiang.hengyang@njust.edu.cn), [caibo@njust.edu.cn](mailto:caibo@njust.edu.cn), [zhili@njust.edu.cn](mailto:zhili@njust.edu.cn), [zhangslvip@njust.edu.cn](mailto:zhangslvip@njust.edu.cn), and [zeng.haibo@njust.edu.cn](mailto:zeng.haibo@njust.edu.cn)

## ABSTRACT

In recent years, perovskite light-emitting diodes (PeLEDs) have developed rapidly with the highest external quantum efficiency exceeding 20%. Their unbalanced carrier injection and non-radiative recombination assisted by defects lead to the destruction of perovskite crystal structures and poor device stability, which hinders their commercialization process. Thus, to understand the origin of device performance, the key is to figure out the charge-carrier dynamics of the devices. In this review, the charge-carrier dynamics of perovskites are discussed, including radiative and non-radiative recombination, together with the various passivation strategies. Second, we focus on the interfacial carrier dynamics and its influence on device performance. Various strategies to improve the injection balance have been implemented to address the inherent challenges associated with PeLEDs. Last but not least, the characterization techniques of PeLEDs are provided to study the carrier dynamics of PeLEDs.

Published under an exclusive license by AIP Publishing. <https://doi.org/10.1063/5.0080087>

## TABLE OF CONTENTS

I. INTRODUCTION .....	1	4. Simulation techniques .....	19
II. CHARGE-CARRIER DYNAMICS FOR MATERIALS ..	3	IV. CONCLUSION AND OUTLOOK .....	20
A. Bimolecular radiative recombination in 3D perovskites .....	3		
B. Monomolecular exciton dynamics in low-dimensional perovskites .....	4		
C. Unexpected non-radiative Auger recombination ..	6		
D. Minimizing the trap-induced non-radiative recombination .....	7		
E. Self-trapping excitons .....	9		
III. CHARGE-CARRIER DYNAMICS FOR PELEDs .....	12		
A. Interface in PeLEDs .....	12	I. INTRODUCTION	
B. Carrier injection balance in PeLEDs .....	12	Perovskites show good application prospects in solar cells, light-emitting diodes (LEDs), lasers, thanks to their various excellent photoelectric properties of, but not limited to, high photoluminescence quantum yields (PLQYs), high carrier mobility, widely tunable bandgap, and easy manufacturing process. <sup>1–9</sup> Although the earliest report on perovskite light-emitting diodes (PeLEDs) can be traced back to 1994, <sup>10</sup> room temperature PeLED is confirmed by Friend's group until 2014, and the device performance is not ideal. <sup>11</sup> After several years of development, the external quantum efficiencies (EQEs) of PeLEDs have exceeded 20%, <sup>12–17</sup> and the PLQYs have reached almost 100%, <sup>18</sup> which is comparable to organic light-emitting diodes (OLEDs) and core-shell quantum dot LEDs (QLEDs). <sup>19–21</sup>	
C. Characterization and simulation techniques of charge-carrier dynamics in PeLEDs .....	14	However, there are still great challenges to assemble PeLEDs into high-performance devices due to the drawbacks of perovskites: (i) perovskites are unstable and extremely sensitive to air, water, and	
1. Mobility characterization techniques .....	16		
2. Defect density characterization technology ...	17		
3. Recombination process characterization techniques .....	18		

temperature, and can produce a large number of structural defects, resulting in non-radiative recombination;<sup>22</sup> (ii) the intrinsic defects in perovskites lead to non-radiative recombination and low PLQYs;<sup>23</sup> and (iii) the imbalance of charge-carrier injection will also lead to a decrease in radiative recombination rate.<sup>24</sup> Therefore, understanding the performance origin of PeLEDs has always been a key subject in research of halide perovskites, which is closely related to the charge-carrier dynamics in PeLEDs.

Theoretically, perovskite crystals with different dimensions have different carrier recombination dynamics due to their different crystal sizes. Specifically, for three-dimensional (3D) perovskites, the low exciton binding energy and long carrier diffusion length make non-radiative recombination superior to radiative recombination.<sup>25–27</sup> Compared with 3D perovskite, low-dimensional perovskites exhibit more excellent luminescence properties due to quantum confinement effect and larger exciton binding energies.<sup>28,29</sup> However, the large exciton binding energy of low-dimensional perovskites will lead to a decrease in mobility. As reported by Hartono *et al.*, the poor

performance of dimensionally reduced devices may be due to the limited out-of-plane charge-carrier mobility, which in turn affects device lifetime.<sup>30</sup> Therefore, it is significant to understand the carrier recombination process of crystalline materials with different dimensions. Furthermore, the carrier behavior of PeLEDs (interfaces) is also an important factor affecting device performance. Understanding the charge-carrier dynamics of the entire device can help achieve more high-performance devices and solve the problems and challenges faced by perovskites.

In this review, the charge-carrier dynamics of materials and interfaces of PeLEDs will be summarized. Initially, three main charge-carrier recombination processes (Fig. 1), including radiative, defect-assisted non-radiative, and Auger recombination, are discussed. For the radiative recombination, electrons (e) and holes (h) directly combine to emit photons, as shown in Fig. 1(a), which is the luminescence mechanism desired in PeLEDs. In defect-assisted non-radiative recombination, e-h pairs recombine through the deep-level defect, releasing the phonons [Fig. 1(b)]. When the carrier density is high, the

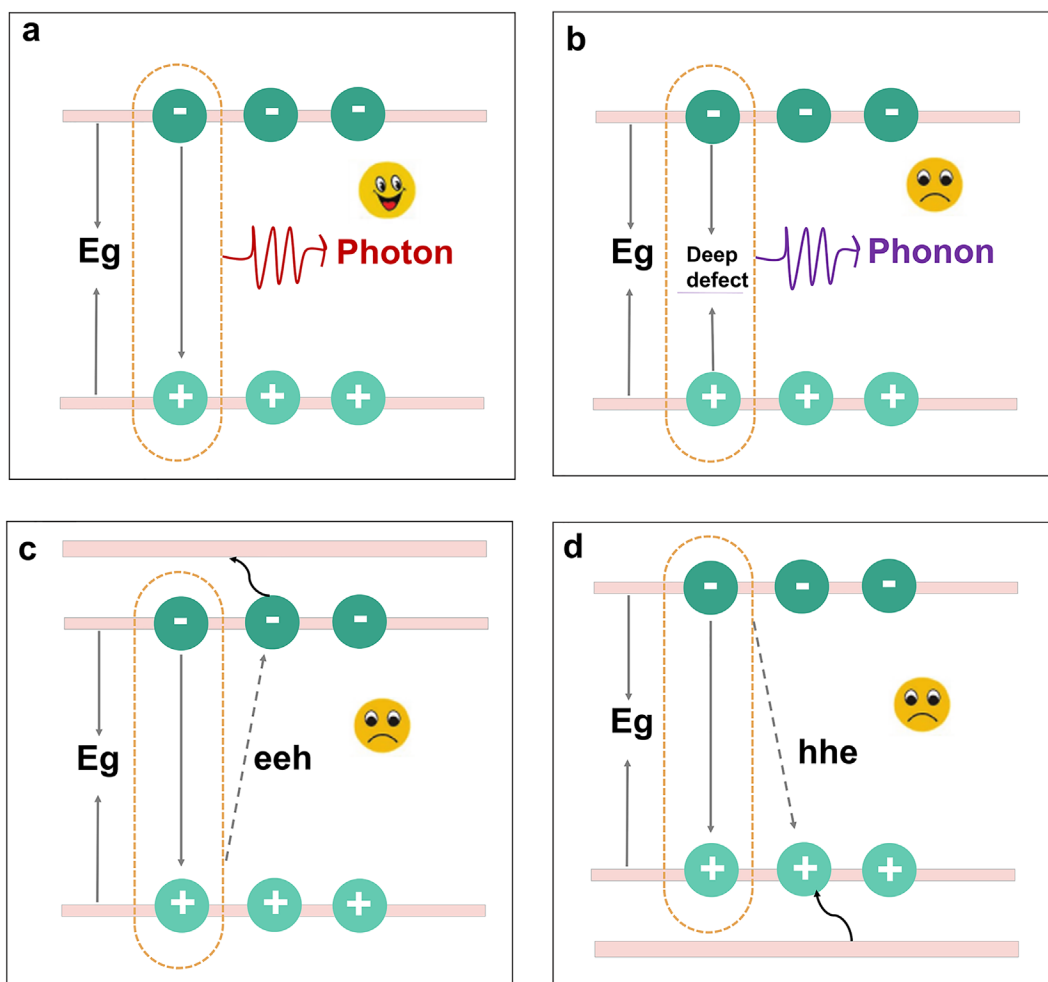


**FIG. 1.** Charge-carrier recombination dynamics: (a) radiative recombination, (b) defect-assisted non-radiative recombination, (c) electron-electron-hole (eeh), and (d) hole-hole-electron (hhe) Auger recombination.

electrons and holes will transfer the excess energy to the third electron or hole, forming electron-electron-hole (eeh) or hole-hole-electron (hhe) tri-molecular Auger recombination, as displayed in Figs. 1(c) and 1(d). In this section, we introduce the three recombination modes from the aspects of three-dimensional (3D) perovskites, low-dimensional perovskites [two-dimensional (2D), quasi-2D, nanocrystals (NCS)], as well as the factors affecting the three recombination processes, and the strategies to improve the PLQYs. In the interface carrier dynamics, we will comprehensively introduce the key factors affecting carrier transport in PeLEDs. Finally, the significant characterization techniques of charge-carrier dynamics in PeLEDs are discussed. These studies reveal the underlying mechanism of the excited state dynamics of PeLEDs.

## II. CHARGE-CARRIER DYNAMICS FOR MATERIALS

The PeLED performance is determined by four factors, including PLQY( $\eta_{PLQY}$ ), efficiency of carrier injection into the emitting layer (EML) ( $\eta_{injection}$ ), light extraction efficiency ( $\eta_{extraction}$ ), and stability ( $\eta_{hold}$ ), respectively, which can be expressed by the following formula:

$$\eta_{PeLED} = \eta_{PLQY} * \eta_{injection} * \eta_{extraction} * \eta_{hold}. \quad (1)$$

According to formula (1), to achieve high-performance PeLEDs, the intrinsic high PLQYs from the luminescent materials themselves are first required, which depends on the result of the competition between radiative and non-radiative recombination processes. The formula of PLQY is as follows:

$$PLQY = \frac{\sum R_r}{\sum R_r + \sum R_{nr}}, \quad (2)$$

where  $R_r$  and  $R_{nr}$  refer to radiative and non-radiative recombination rates, respectively. According to formula (2), increasing the radiative rate or decreasing the non-radiative rate is instrumental in improving PLQYs. Radiative recombination consists of two processes, one is the bimolecular radiative recombination process, and the other is the monomolecular exciton recombination.<sup>31,32</sup> Non-radiative recombination also contains two processes, one is non-radiative recombination assisted by defects and the other is tri-molecular Auger recombination.<sup>33,34</sup>

In this section, we focus on the charge-carrier recombination dynamics of 3D and low-dimensional perovskites, and the strategies to control the non-radiative recombination of perovskites to obtain high PLQYs. In addition, the self-trapping excitons (STEs) luminescence of perovskites are discussed from four aspects: structural dimension regulation, doping ion regulation, chemical composition regulation, and phase transition.

### A. Bimolecular radiative recombination in 3D perovskites

3D perovskites usually have small exciton binding energies ( $\approx 30\text{--}76\text{ meV}$ ) close to room temperature thermal energy ( $k_B T \approx 25\text{ meV}$ ),<sup>29,35</sup> which indicates that the excitons in the perovskites are easily dissociated into free charge-carriers, that is, electrons and holes recombine in a bimolecular combination. The charge-carrier recombination dynamics in 3D perovskites can be described by the following equation:<sup>36-38</sup>

$$-\frac{dn}{dt} = An + Bn^2 + Cn^3, \quad (3)$$

where  $n$  is the charge-carrier density,  $t$  is the time,  $A$ ,  $B$ , and  $C$  are coefficient of the non-radiative, radiative, and Auger recombination, respectively. Note that the equations all assume that the injection of electrons and holes are equal.<sup>39</sup> According to formula (3),  $n$  values and coefficients ( $A$ ,  $B$  and  $C$ ) are related to charge-carrier dynamics of 3D perovskites. At low carrier densities, the charge-carriers are easily trapped by defects forming non-radiative recombination. In Fig. 2(a), trap saturation can also be seen at relatively high carrier densities, in which case, radiative recombination is dominant. The PLQYs of 3D perovskites can be expressed by the following equation:

$$PLQY = \frac{Bn}{A + Bn + Cn^2}. \quad (4)$$

Figures 2(b) and 2(c) show the relationship between PLQYs and carrier densities in different coefficients  $B$  and  $A$ . As is known to all, the carrier densities in 3D perovskites electroluminescent (EL) devices are generally lower than  $10^{15}\text{ cm}^{-3}$ .<sup>40</sup> When the intrinsic parameters of  $A = 10^6\text{ s}^{-1}$  and  $C = 10^{-28}\text{ cm}^6\text{ s}^{-1}$  are fixed, PLQYs gradually increase with the increase in coefficients  $B$ . When  $n = 10^{15}\text{ cm}^{-3}$ , the maximum PLQY can reach more than 80% at  $B = 5 \times 10^{-9}\text{ (cm s}^{-1})$ . However, the  $B$  value reported in the literatures is around  $1 \times 10^{-10}\text{ cm}^3\text{ s}^{-1}$ , and the maximum PLQY can only reach about 10% from Fig. 2(b). When the intrinsic parameters of  $B = 10^{-10}\text{ cm}^3\text{ s}^{-1}$  and  $C = 10^{-28}\text{ cm}^6\text{ s}^{-1}$  are fixed, decreasing the values of  $A$  from  $1 \times 10^7\text{ s}^{-1}$  to  $1 \times 10^4\text{ s}^{-1}$  can increase PLQYs from 1% to 90% at  $n = 10^{15}\text{ cm}^{-3}$ . Although the PLQY can reach 90%, the literature reported  $A$  value of about  $10^7\text{ s}^{-1}$ , PLQY is less than 10% at  $n = 10^{15}\text{ cm}^{-3}$ .

Although the performance of 3D PeLEDs is limited due to the slow bimolecular radiative recombination rates under the low carrier densities [Figs. 2(b) and 2(c)], the radiative recombination rate can be increased by reducing the size of 3D perovskites to confine the free carriers. Back in 2014, Friend and his team designed an ultra-thin perovskite structure with a thickness of 30 nm to spatially limit electrons and holes and improve the radiative recombination rate, eventually achieving the first room-temperature PeLED, albeit with a very low PLQY.<sup>11</sup> Subsequently, Lee *et al.* blocked the formation of metallic lead, which promotes exciton quenching, by adding the molar ratio of methylammonium bromide (MABr), and restricted excitons to methylammonium lead bromide ( $\text{MAPbBr}_3$ ) with a diameter of about 100 nm, significantly increasing PLQY from 3% to 36%.<sup>41</sup> In 2017, Rand *et al.* significantly limited the growth of 3D methylammonium lead bromide and iodide systems, resulting in a 40.1% PLQY for Br-perovskite film and a 6.6% PLQY for I-perovskite film.<sup>42</sup> Recently, Tang and his group proposed the strategy of introducing zero-dimensional (0D)  $\text{Cs}_4\text{PbBr}_6$  into 3D  $\text{CsPbBr}_3$  [Fig. 2(d)] and obtained core-shell like structures  $\text{CsPbBr}_3/\text{Cs}_4\text{PbBr}_6$  with different Cs/Pb ratios, which improved the radiative recombination rate of 3D perovskite films through space confinement. The charge-carrier dynamics are studied by transient absorption, as shown in Fig. 2(e). As a result, the radiative rate  $k_2$  increases from  $1.47 \times 10^{-10}$  to  $9.34 \times 10^{-10}\text{ cm}^3\text{ s}^{-1}$ , and the non-radiative recombination rate  $k_1$  decreases from  $1.69 \times 10^9$  to  $7.14 \times 10^8\text{ s}^{-1}$ . As expected, PLQY (40.8%) with  $\text{Cs}/\text{Pb} = 1.56$  is higher than PLQY (21.5%) with  $\text{Cs}/\text{Pb} = 1.24$ .<sup>43</sup> In particular, Deschler *et al.* recently proposed a new concept to increase PLQY

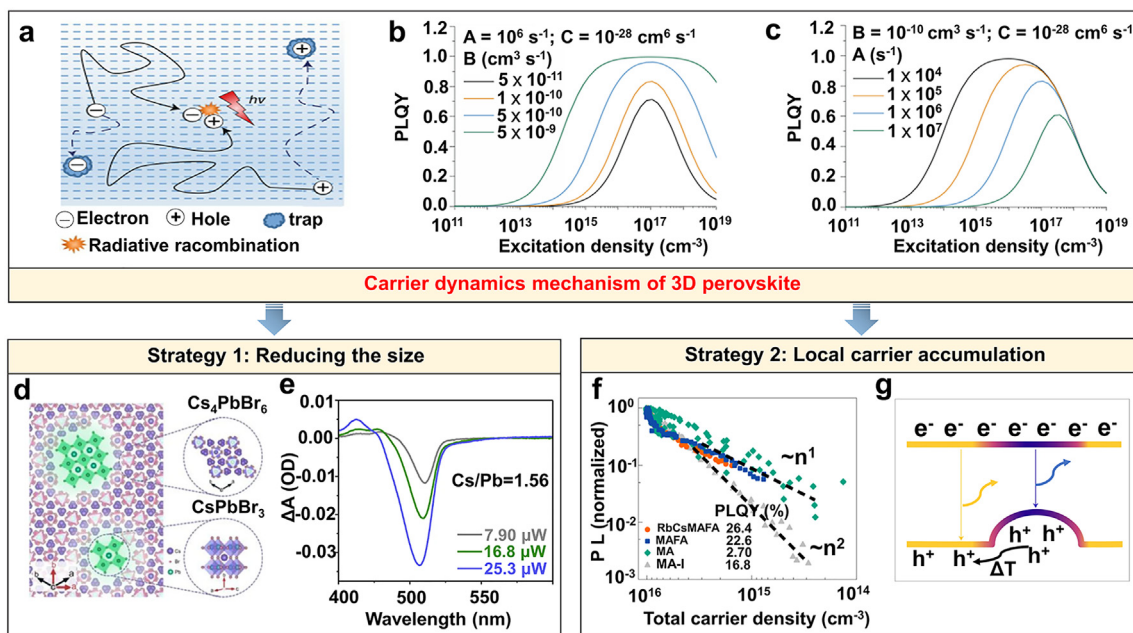


**FIG. 2.** Charge-carrier recombination dynamics for 3D perovskites. (a) Mechanism diagram of electrons and holes recombination. (b) The function relationship of PLQY-excitation density in different coefficients B. (c) The function relationship of PLQY-excitation density in different coefficients A. Reproduced with permission from Gao *et al.*, Nat. Mater. **20**, 10 (2021). Copyright 2021 Nature Publishing Group.<sup>36</sup> (d) The structure diagram of 0D Cs<sub>4</sub>PbBr<sub>6</sub> adds to 3D CsPbBr<sub>3</sub>. (e) The transient absorption spectra at Cs/Pb = 1.56 under the various excitation fluences. Reproduced with permission from Tang *et al.*, Nat. Commun. **12**, 4751 (2021). Copyright 2021 Nature Publishing Group.<sup>43</sup> (f) Schematic diagram of PL as a function of total carrier density. MA-I belongs to the second-order recombination, while first-order recombination behavior has been observed in other compounds, resulting in high PL at low carrier density. (g) Schematic diagram of local accumulation of charge-carriers. Reproduced with permission from Stranks and Deschler *et al.*, Nat. Photonics **14**, 123 (2019). Copyright 2019 Nature Publishing Group.<sup>44</sup>

through local charge-carrier accumulation. Transient photoluminescence spectroscopy revealed that the transition from second-order non-radiative recombination to first-order radiative recombination can be made by regulating the local charge-carriers of band edge [Figs. 2(f) and 2(g)], which provides a strategy for improving PLQY and implementing the high-performance devices.<sup>44</sup>

## B. Monomolecular exciton dynamics in low-dimensional perovskites

PLQYs can be improved not only by enhanced bimolecular radiative recombination but also by monomolecular radiative recombination. Compared with 3D perovskites, low-dimensional perovskites (2D, quasi-2D, NCs) have quantum confinement effect and large exciton binding energy ( $E_b$ ),<sup>5</sup> which result in a rapid monomolecular radiative recombination. Therefore, the excited state of low-dimensional perovskites is no longer free carriers, but exists in the form of excitons, as shown in Fig. 3(a).<sup>36</sup> Figure 3(b) shows the function of PLQYs and excitation densities for 3D and quasi-2D perovskites,<sup>32</sup> finding that quasi-2D perovskites exhibit higher PLQYs than 3D perovskites at low charge-carrier density. Therefore, the recombination dynamics of excitons and free-carriers are completely different. In low-dimensional perovskites, the radiative and non-radiative recombination are both monomolecular recombination processes, while Auger recombination is a bimolecular recombination process.

The charge-carrier dynamics of low-dimensional perovskites can be described by the following formulas:

$$-\frac{dn}{dt} = (A + B)n + Cn^2, \quad (5)$$

$$\text{PLQY} = \frac{B}{(A+B)+Cn}. \quad (6)$$

Among them, A, B, and C are the rate constants of non-radiative, radiative, and Auger recombination, respectively. According to formula (6), at the low excitation density, PLQY = B/(A + B), regardless of carrier density [Fig. 3(c)].<sup>36</sup> Although radiative and non-radiative recombination processes are competitive, the exciton radiative recombination may be dominant, provided that the inherent defects of the materials are well passivated (B ≥ A).

For 2D perovskites ( $n = 1$ ) [Fig. 3(d)], although there is an obvious quantum confinement effect and large exciton binding energy, the high defect density makes the excited state quench fast, resulting in a low PLQY (~0.5%) and a shorter PL lifetime of about 40 ps.<sup>45</sup> A quasi-2D structure with multiple quantum wells (MQW) would be obtained when  $n > 1$ , together with the energy transfer spontaneously [Fig. 3(e)].<sup>46,47</sup> In this case, the process of  $n = 1$  is no longer important, and the energy will be transferred out before quenching. There is a cooperative confinement system of dielectric and quantum confinement in quasi-2D perovskites, which can effectively improve the recombination rate of excitons. However, serious non-radiative recombination exists in the energy transfer process, which limits the luminescence performance. Given this, Yang *et al.* used methanesulfonate (MES) additive to smooth the energy transfer path by reconstructing the structure and reducing defect states, resulting in an increasing in

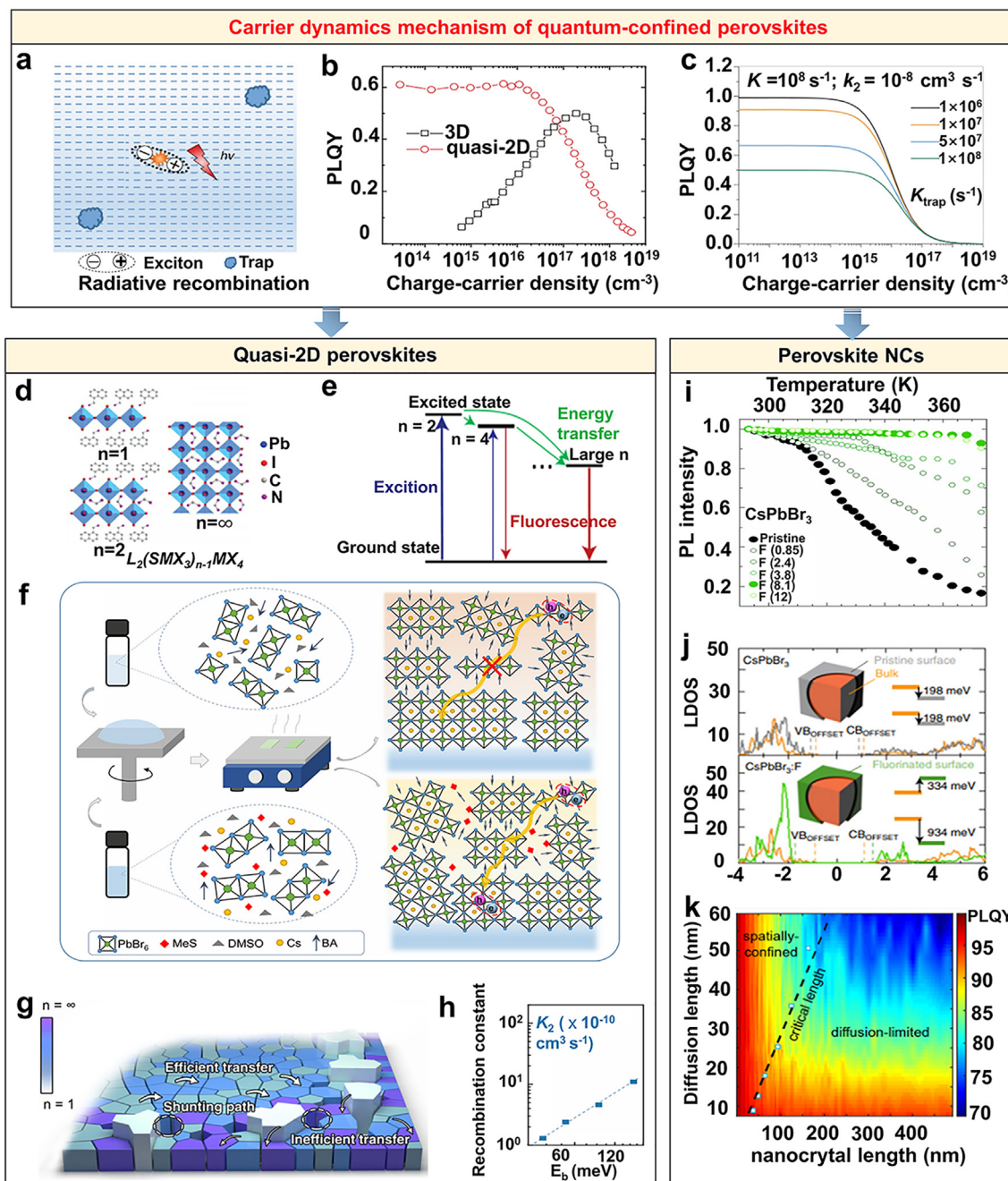


**FIG. 3.** Charge-carrier dynamics of low-dimensional perovskites. (a) Schematic diagram of charge-carrier recombination. Reproduced with permission from Gao *et al.*, Nat. Mater. **20**, 10 (2021). Copyright 2021 Nature Publishing Group.<sup>36</sup> (b) The relationship between PLQY and carrier density of 3D and quasi-2D perovskites. Reproduced with permission from Huang *et al.*, Nat. Commun. **8**, 14558 (2017). Copyright 2017 Nature Publishing Group.<sup>32</sup> (c) Related PLQY-excitation density plots with different trap-assisted non-radiative recombination rate constants  $K_{\text{trap}}$  ( $\text{s}^{-1}$ ). Reproduced with permission from Gao *et al.*, Nat. Mater. **20**, 10 (2021). Copyright 2021 Nature Publishing Group.<sup>36</sup> (d) Schematic diagram of perovskite structures in  $n=1$ ,  $n=2$ , and  $n=\infty$ . (e) Mechanisms of energy transfer in quasi-2D perovskites. Reproduced with permission from Wang and Huang *et al.*, Nat. Photonics **10**, 699 (2016). Copyright 2016 Nature Publishing Group.<sup>47</sup> (f) Effects of methanesulfonate (MeS) additive on phase distribution of  $\text{BA}_2\text{Cs}_{n-1}\text{Pb}_n\text{Br}_{3n+1}$  films. Reproduced with permission from Rogach and Yang *et al.*, Nat. Commun. **12**, 1246 (2021). Copyright 2021 Nature Publishing Group.<sup>48</sup> (g) The diagram shows the phase separation of quasi-2D perovskite and the corresponding non-radiative loss path. (h) The recombination constant as a function of  $E_b$ . Reproduced with permission from Yuan *et al.*, Nat. Commun. **12**, 2207 (2021). Copyright 2021 Nature Publishing Group.<sup>49</sup> (i) PL decay curves of pristine and different fluorine/bromo percentages  $\text{CsPbBr}_3$  NCs. (j) Local density of states (LDOSs) of bulk and surface layers of pristine  $\text{CsPbBr}_3$  (upper) and fluoride ions occupying all bromide-ion positions (lower). Reproduced with permission from Li *et al.*, Nat. Photonics **15**, 379 (2021). Copyright 2021 Nature Publishing Group.<sup>58</sup> (k) Schematic diagram of PLQY in nanocrystals in relation to diffusion length and size. Reproduced with permission from Yang *et al.*, J. Am. Chem. Soc. **142**, 8871 (2020). Copyright 2020 American Chemical Society.<sup>33</sup>

the proportion of large  $n$  phases with narrow bandgap quantum wells. The PLQY increased from 47% to 73% [Fig. 3(f)].<sup>48</sup> Indeed, a series of quasi-2D perovskites have exhibited excellent PLQYs in PeLEDs due to their quality optical properties.<sup>48–52</sup> However, when the size increases, defects increase and PLQY decreases, which may be caused by phase separation. Thus, Yuan *et al.* proposed an “intermediate phase regulation” strategy and introduced L-Norvaline (NVAL) to inhibit phase segregation [Fig. 3(g)]. They are surprised to find that the nucleation crystallization of film starts from quasi-2D rather than 3D perovskite phases, which significantly inhibits phase separation and obtains high-quality and large-area quasi-2D perovskite films with a high PLQY of ~80%. The relationship between  $E_b$  and recombination constant shows that the radiative recombination rate  $k_2$  increases with the increase in  $E_b$  [Fig. 3(h)]. Therefore, the radiative recombination of excitons can be improved by increasing  $E_b$ .<sup>49</sup>

Perovskite NCs are usually divided into quantum dots (QDs), nanorods, nanowire, and nanosheets according to their morphologic differences. Due to their quantum confinement effect and large exciton binding energy, PLQYs have been significantly improved. Since the synthesis of some early perovskite QDs, the PLQYs have reached 50%–85%, and there are many strategies to improve PLQY, such as halogen composition regulation and doping, making the PLQY of perovskite close to 100%.<sup>18,53–57</sup> It is known that PLQY decreases with the occurrence of thermal quenching, which hinds the practical application of perovskite NCs in EL diodes. Very recently, Li *et al.* obtained the PL spectra of CsPbBr<sub>3</sub> NCs with different fluorine/bromo percentages through fluoride post-treatment, and found that the luminescence of CsPbBr<sub>3</sub> NCs in fluorine (8.1) is not affected at a temperature of up to 373 K, and the fluorescence performance is nearly zero quenching [Fig. 3(i)]. The calculations of electronic structures show that the local density of states (LDOSs) of CsPbBr<sub>3</sub> NCs changed from type-II to type-I after fluorine treatment, which is beneficial to luminescence, as shown in Fig. 3(j).<sup>58</sup> Although the above analysis found that low-dimensional perovskites are conducive to higher PLQYs, the quantitative understanding of the dimensions is still unclear. Yang *et al.* developed a quantitative model to account for the effects of carrier diffusion and material dimension on carrier recombination dynamics and luminescence efficiency, as shown in Fig. 3(k).<sup>33</sup> It is found that the smaller the nanocrystalline length and diffusion length, the larger the PLQY. When the nanocrystal length is less than 50 nm, PLQY is large, which is independent of the diffusion length. When the diffusion length is less than 20 nm, PLQY is large regardless of nanocrystal length.

However, excitons have the potential to dissociate into free carriers during the radiative recombination process described above, limiting luminescence. Mohite *et al.* found exciton dissociation in quasi-2D perovskites with  $E_b$  values of several hundred meV.<sup>59</sup> Therefore, understanding the intrinsic mechanism of exciton dissociation is of great significance for PeLEDs. Yang *et al.* declared that electron coupling energy and  $E_b$  have a strong influence on exciton dissociation in perovskite NCs. When the  $E_b$  is greater than the electronic coupling energy, the excitons play a dominant role, which is beneficial to the radiative recombination mechanism of PeLEDs.<sup>60</sup> Wright *et al.* suggested that in quasi-2D (PEA)<sub>2</sub>(CH<sub>3</sub>NH<sub>3</sub>)<sub>n-1</sub>Pb<sub>n</sub>I<sub>3n+1</sub> ( $n = 1, 2, 3, 4$ , and  $\infty$ ), the recombination rate increases with the increase in  $n$ , but when  $n > 4$ , the exciton dissociates into free carriers and the recombination rate decreases.<sup>61</sup> Thus, the exciton binding energy is larger in

the moderate  $n$ -valued quasi-2D perovskite phase, which ensures effective exciton recombination. In the high  $n$ -valued phase, excitons tend to dissociate into free carriers and exciton binding energy decreases.

### C. Unexpected non-radiative Auger recombination

Although PLQYs can be increased by reducing the dimensions, Auger recombination is inevitable. Auger recombination is a non-radiative process, and the excess energy is transferred to another electron or hole to form eeh, or hhe tri-molecular Auger recombination [Fig. 4(a)], which results in exciton emission quenching. For 3D perovskites, the C value is about  $10^{-28} \text{ cm}^6 \text{ s}^{-1}$ ,<sup>62</sup> and the Auger recombination only dominates when the concentration is greater than  $10^{17} \text{ cm}^{-3}$  [Fig. 2(b)], indicating that the Auger recombination can be ignored and it is promising for high-brightness PeLEDs. In quasi-2D perovskites, the high  $E_b$  will seriously affect the local uniformity of carriers in the material, leading to Auger recombination [Fig. 4(b)], which ultimately severely inhibits the stability and brightness of PeLEDs under high current operation, and restricts the further commercialization process of quasi-2D perovskites in the PeLEDs. Therefore, in order to reduce the Auger recombination rate of quasi-2D perovskite, Yuan *et al.* proposed to replace the long-chain organic amine phenethylammonium (PEA) with highly polar organic amine *p*-fluorophenethylammonium (*p*-FPEA), hoping to reduce the  $E_b$  in the quasi-2D perovskite film and thus achieve a higher Auger recombination threshold. Surprisingly, compared with PEA, *p*-FPEA has a small  $E_b$  [Fig. 4(c)], and further global fitting of the correlated transient absorption spectra shows that Auger recombination constant  $k_3$  decreases from  $7.9 (\pm 2.1) \times 10^{-27}$  to  $3.2 (\pm 0.9) \times 10^{-28} \text{ cm}^6 \text{ s}^{-1}$ . Unfortunately, PLQY also decreased from 66% (PEA) to 51% (*p*-FPEA). Therefore, they further used potassium trifluoromethane-sulfonate (CF<sub>3</sub>KO<sub>3</sub>S) to passivate the defects, making the PLQY almost unchanged (85% vs 82%).<sup>63</sup>

Notably, the Auger recombination of 3D perovskites only occurs at high charge-carrier density [Fig. 2(b)], so we generally do not study the Auger recombination of 3D perovskites. Although NCs and 3D perovskites have the same structure, their Auger recombination mechanism is different, in which 3D materials need to meet the momentum and energy conservations, while NCs only need energy conservation due to its discrete energy level structure. Thus, the Auger recombination rate should decay exponentially with the  $E_g$  in 3D materials [Fig. 4(d), left]. In NCs, Auger recombination occurs efficiently for band edge carriers [Fig. 4(d), right], which is independent of  $E_g$ .<sup>64</sup> Thus, to understand the internal mechanism of Auger recombination, the size and composition of NCs are necessary for accurate determination of Auger recombination lifetimes. To this end, Wu *et al.* reported the synthesis of APbX<sub>3</sub> (A = Cs, FA; X = Cl, Br, I), and the systematic test of the Auger lifetime, the results show that the biexciton Auger lifetime is not related to the cation, but dependent on the halide ion, in which the scaling coefficient of Cl, Br and I are 0.035, 0.085 and 0.142 ps nm<sup>-3</sup>, respectively. These results are faster than that of standard CdSe and PbSe materials, about ~1 ps nm<sup>-3</sup>, suggesting the Auger lifetimes of perovskite NCs are shorter than standard NCs, as exhibited in Fig. 4(e).<sup>64</sup>

We know that the carriers maintain the same phase after the initial excitation. However, perovskites have a short coherence time due to the strong electron-phonon (e-ph) coupling. For example, the

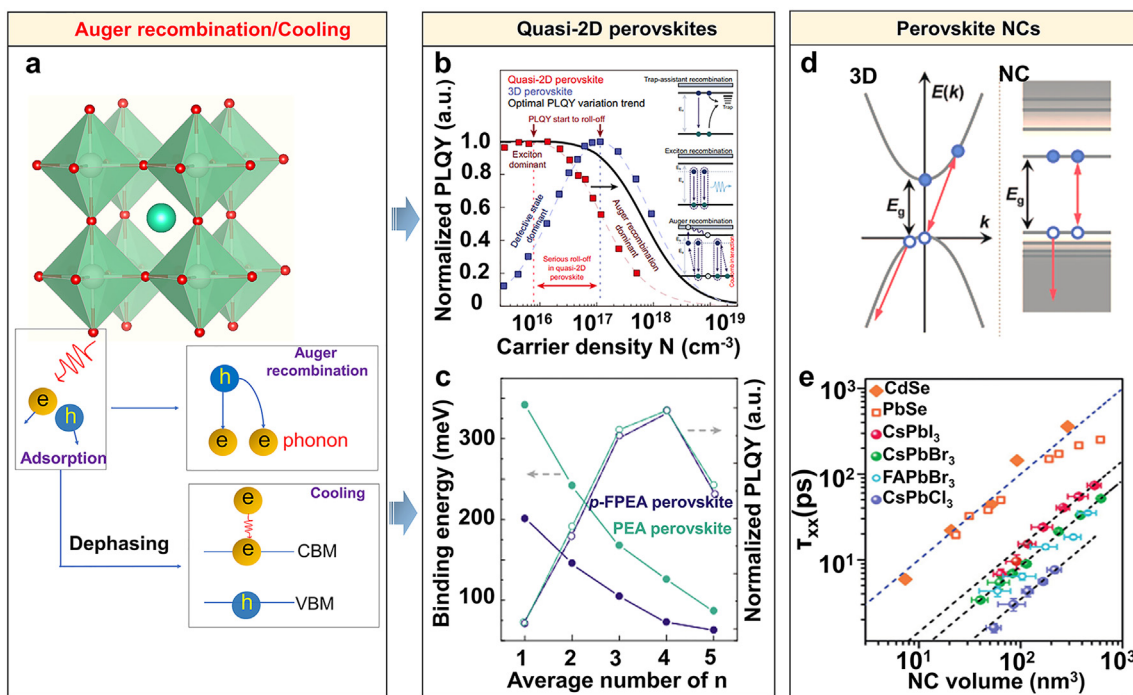


**FIG. 4.** (a) Charge-carrier Auger recombination and cooling process. (b) Experimental PLQY variation with charge-carrier density for quasi-2D and 3D perovskite films. (c) Extracted  $E_b$  corresponding PLQYs for PEA and *p*-FPEA based on quasi-2D films with different  $n$  values. Reproduced with permission from Yuan *et al.*, Nat. Commun. **12**, 336 (2021). Copyright 2021 Nature Publishing Group.<sup>63</sup> (d) The difference of bulk (left) and NC (right) materials in Auger recombination processes. (e) Auger lifetimes of several NCs as a function of NC volume. Reproduced with permission from Wu *et al.*, Angew. Chem. Int. Ed. **59**, 14292 (2020). Copyright 2020 Wiley-VCH.<sup>64</sup>

decoherence time of 3D  $\text{CH}_3\text{NH}_3\text{PbI}_3$  is 220 fs.<sup>65</sup> In quantum well materials, the decoherence time decreases rapidly with the decrease in the well.<sup>66</sup> After dephasing, carrier cooling occurs, as shown in Fig. 4(a), which is directly related to the luminescence efficiency.<sup>67–69</sup> During the cooling process, hot electrons need to scatter with phonons and transfer energy into the lattice. In the bulk phases, the relaxation rate of hot electrons is fast, and can usually relax to the band edge at the femtosecond level, e.g., the relaxation lifetime of  $\text{MAPbI}_3$  is within 100 fs<sup>70</sup> and  $\text{FAPbI}_3$  is about 300 ps at high photoexcitation.<sup>71</sup> Inversely, for low-dimensional materials, the relaxation rate of hot electrons is reduced to some extent due to the splitting of continuous energy level positions, and multiple phonons need to be coupled simultaneously to achieve relaxation. This phenomenon is called phonon bottleneck.<sup>70</sup> It is found that the hot phonon bottleneck effect in perovskites can reduce the cooling rate of carriers by 3–4 orders of magnitude.<sup>72</sup> However, in 2018, Han and his team synthesized  $\text{Cs}_2\text{AgBiX}_6$  ( $X = \text{Cl}, \text{Br}, \text{I}$ ) NCs with cubic phase for the first time, and found that the hot carriers cooling is ultra-fast, less than 1 ps, indicating that the non-lead NCs with ultra-fast carrier cooling lifetime are expected to be a potential material for PeLEDs.<sup>69</sup>

#### D. Minimizing the trap-induced non-radiative recombination

Passivation defect is an important strategy to improve PLQYs in 3D and low-dimensional perovskites.<sup>23</sup> Defects in perovskites include

uncoordinated halogen ion ( $\text{X}^-$ ), uncoordinated lead ion ( $\text{Pb}^{2+}$ ), 3D defect (Pb cluster), and point defects, which consist of vacancies, interstitials and anti-site occupations [Fig. 5(a)].<sup>36</sup> Theoretical calculations [Fig. 5(b)] show that<sup>73</sup> low formation energy defects include interstitial defects ( $\text{I}_i$  and  $\text{MA}_i$ ), vacancy defects ( $\text{V}_i$ ,  $\text{V}_{\text{MA}}$ , and  $\text{V}_{\text{Pb}}$ ) and anti-site occupations defects ( $\text{MA}_{\text{Pb}}$ ,  $\text{Pb}_{\text{MA}}$ , and  $\text{MA}_{\text{l}}$ ) in  $\text{MAPbI}_3$ , which are all shallow level defects. Deep level defects ( $\text{Pb}_i$ ,  $\text{I}_{\text{MA}}$ ,  $\text{I}_{\text{Pb}}$ , and  $\text{Pb}_{\text{l}}$ ) have relatively high formation energy and are difficult to form. These defects can lead to undesirable non-radiative recombination, reducing PLQYs.

Various effective defect passivation strategies have been developed to reduce defect density and increase radiative recombination.<sup>74</sup> It is well known that defects inevitably lead to electricity, when perovskite is negatively charged, such as  $\text{I}^-$ , we can neutralize defects by introducing metal cations ( $\text{Na}^+$ ,  $\text{K}^+$ ,  $\text{Rb}^+$ , etc.)<sup>75,76</sup> [Fig. 5(c)] to form ionic bonds, or by Lewis acid (halogen bond donor) through coordination bond.<sup>77,78</sup> For example, Snaith *et al.* reported the Lewis acid passivator iodopentafluorobenzene (IPFB), in which F has the strongest electronegativity, and the electron clouds run toward F, while the electron cloud density of I decreases. Then, I and  $\text{X}^-$  ( $\text{I}^-$ ,  $\text{Br}^-$ ,  $\text{Cl}^-$ ) form halogen bonding  $-\text{C}-\text{I}\cdots\text{X}^-$  to passivate the uncoordinated halogen anions [Fig. 5(d)].<sup>79</sup> In addition, divalent metal cations ( $\text{Mn}^{2+}$ ,  $\text{Cd}^{2+}$ ,  $\text{Ni}^{2+}$ ,  $\text{Ca}^{2+}$ ,  $\text{Sn}^{2+}$ )<sup>80–83</sup> and trivalent metal cations ( $\text{Al}^{3+}$ ,  $\text{In}^{3+}$ ,  $\text{Bi}^{3+}$ ,  $\text{Sb}^{3+}$ ,  $\text{Eu}^{3+}$ )<sup>84–87</sup> also have passivation effects. Organic cations, such as phenethylammonium iodide (PEAI), can also passivate negative charge defects thereby reducing surface defects and inhibiting

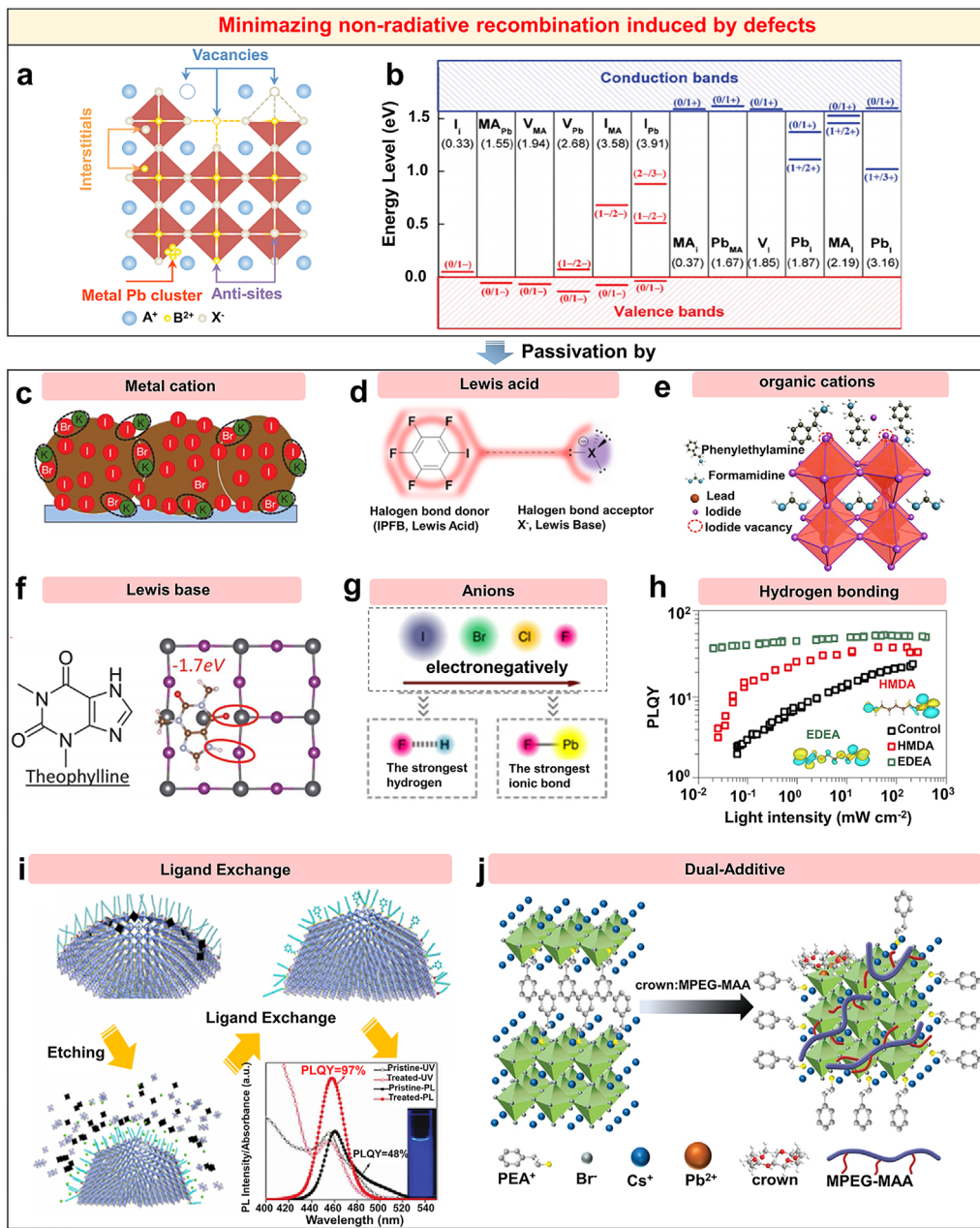


**FIG. 5.** Defects and defect passivation strategies of perovskites. (a) Types of point defects, including vacancies, interstitials, anti-site occupations and Pb cluster. Reproduced with permission. Reproduced with permission from Gao et al., Nat. Mater. **20**, 10 (2021). Copyright 2021 Nature Publishing Group.<sup>36</sup> (b) Band alignment of different defects. Reproduced with permission from Yan et al., Adv. Mater. **26**, 4653 (2014). Copyright 2014 Wiley-VCH.<sup>73</sup> (c) K<sup>+</sup> passivates undercoordinated I<sup>-</sup> and Br<sup>-</sup> between grain boundaries and surfaces by forming ionic bonds. Reproduced with permission from Friend and Stranks et al., Nature **555**, 497 (2018). Copyright 2018 Nature Publishing Group.<sup>75</sup> (d) Schematic diagram of the interaction between Lewis acid passivator iodopentafluorobenzene (IPFB) and X<sup>-</sup> (I<sup>-</sup>, Br<sup>-</sup>, Cl<sup>-</sup>). Reproduced with permission from Snaith et al., Nano Lett. **14**, 3247 (2014). Copyright 2014 American Chemical Society.<sup>79</sup> (e) Passivation mechanism via organic cation PEAI for the perovskite film. Reproduced with permission from You et al., Nat. Photonics **13**, 460 (2019). Copyright 2019 Nature Publishing Group.<sup>88</sup> (f) Theoretical model of passivation of (FAPbI<sub>3</sub>)<sub>x</sub>(MAPbBr<sub>3</sub>)<sub>1-x</sub> surface by theophylline. Reproduced with permission from Yang et al., Science **366**, 1509 (2019). Copyright 2019 AAAS.<sup>91</sup> (g) Hydrogen and ionic bond strengths increase with increasing electronegativity. Reproduced with permission from Zhou et al., Nat. Energy **4**, 408 (2019). Copyright 2019 Nature Publishing Group.<sup>92</sup> (h) PLQY as a function of light intensity in control, EDEA and HMDA systems. Inset: Electronic distributions of EDEA and HMDA. Reproduced with permission from Gao et al., Nat. Photonics **13**, 418 (2019). Copyright 2019 Nature Publishing Group.<sup>15</sup> (i) Schematic diagram of acid etching method for driving ligand exchange. The lower right corner shows the relationship of PL intensity and absorption wavelength in pristine and treated QDs. Reproduced with permission from Tian et al., Adv. Mater. **33**, 2006722 (2021). Copyright 2021 Wiley-VCH.<sup>97</sup> (j) Schematic diagram of passivation defects with dual additives crown and MPEG-MAA. Reproduced with permission from Su et al., Adv. Mater. **33**, 2103268 (2021). Copyright 2021 Wiley-VCH.<sup>99</sup>

non-radiative recombination [Fig. 5(e)].<sup>88</sup> The positive charge defects are mainly uncoordinated  $\text{Pb}^{2+}$ , and iodine vacancies on the surface, which can be neutralized by Lewis base (halogen bond acceptor) coordination<sup>89,90</sup> or the introduction of anions. For example, Yang *et al.* systematically investigated the interaction of theophylline, caffeine, and theobromine with perovskite surface defects. When the NH and C=O of theophylline molecules are in the optimal configuration, Pb defects can be effectively passivated by combining with C=O [Fig. 5(f)].<sup>91</sup> The most widely used anionic passivators are halogen anions ( $\text{F}^-$ ,  $\text{Cl}^-$ ,  $\text{Br}^-$ ,  $\text{I}^-$ ). Li *et al.* used  $\text{F}^-$  as an anion passivator, where F would form a hydrogen bond ( $\text{N}-\text{H}\cdots\text{F}$ ) with MA/FA, making perovskite more stable [Fig. 5(g)].<sup>92</sup> Gao and his co-workers systematically studied the competitive mechanism of hydrogen bond formation and passivation effect of passivation molecules, named 2,2'-(ethylenedioxy) diethylamine (EDEA) and hexa-methylenediamine (HMDA), through experimental characterizations and theoretical calculations. The results suggest that the passivation effect of 3D perovskite films can be significantly improved, thus enhancing PLQY in both EDEA and HMDA systems. However, because the electrons of EDEA are evenly distributed at nitrogen atoms and oxygen atoms, the electron-donating capacity and corresponding hydrogen bonding capacity of the amino group are reduced, making the PLQY of EDEA larger than that of HMDA, as shown in Fig. 5(h).<sup>15</sup> In addition, bonds with P=O and As=O terminals have higher binding energies with Pb, obtaining a higher PLQYs.<sup>93</sup> These passivation methods can eliminate only one defect (positive or negative charge), but in most cases both defects may coexist in the prepared perovskite films. Therefore, it is important to explore more effective passivation strategies for these two defects. Xiao *et al.* achieved dual passivation of lead and halogen defects by designing and synthesizing dual passivator 4-fluorophenylmethyldiammonium-trifluoroacetate (FPMATFA), in which TFA anions and FPMA cations combine with unpaired lead and halogen defects, respectively.<sup>94</sup>

Ligand exchange is considered to be an effective strategy to improve the luminescence properties and stability for perovskite NCs.<sup>95,96</sup> Ligands on the surface of perovskite NCs can reduce the surface energy, stabilize the NCs, and prevent the agglomeration of adjacent QDs. However, common ligands, such as oleamine (OAm) and oleic acid (OA), severely limit the carrier injection efficiency of NCs due to their long-chain lengths and poor thermal stability. To this end, Tian *et al.* designed a novel acid etching driven ligand exchange strategy to obtain ultra-low defect density  $\text{CsPbBr}_3$  perovskite QDs. The strategy is to first etch the imperfect  $[\text{PbBr}_6]^{4-}$  octahedron using acid hydrogen bromide (HBr) to remove surface defects. The PLQY is nearly 100% by introducing didodecylamine and phenethylamine to exchange with the original long chain organic ligand, as shown in Fig. 5(i).<sup>97</sup> Core/shell NCs with low attenuation efficiency can also be designed for PeLEDs. Yang *et al.* realized different core/shell  $\text{FAPbBr}_3/\text{CsPbBr}_3$  nanocrystalline structures by regulating process parameters and components. Carrier dynamics show that the PL lifetime of  $\text{FAPbBr}_3/\text{CsPbBr}_3$  nanoparticles is the same as that of PLQY with the increase in X (X are the different molar ratio of Cs/FA), and PLQY is up to 93%.<sup>98</sup> Most recently, Su *et al.* added 18-crown-6 and poly(ethylene glycol) methyl ether acrylate (MPEG-MAA) to PEABr: $\text{CsPbBr}_3$  perovskite films and found that C-O-C bond can not only effectively reduce perovskite defects, but also destroy the self-aggregation of organic ligands and induce the formation of perovskite

NCs with quasi-core/shell structure [Fig. 5(j)]. As a result, the PLQY increased from 12% to 78%.<sup>99</sup>

The influence of perovskite material defects on e-h combination is a key scientific problem in the PeLEDs field. The above discussion is only from the experimental point of view to obtain the results of representation, to understand the internal mechanism of e-h recombination needs the assistance of theoretical calculations. Zhao and her co-workers studied the effect of defects in  $\text{MAPbI}_3$  on e-h non-radiative recombination by using independently developed first-principle excited state dynamics software Hefei-NAMD,<sup>100</sup> and accurately considered the e-ph coupling, electron decoherence and carrier concentration.<sup>101</sup> Figure 6(b) shows the energy levels of valence band maximum (VBM), conduction band minimum (CBM) and defect states at 300 K, and find that only  $\text{I}_i$  and  $\text{MA}_{\text{Pb}}$  have shallow defect states close to the band edges. After photoexcitation, e-ph coupling can induce direct non-radiative recombination of electrons and holes, or by-defect non-radiative recombination mediated by defect states. The dynamics of direct and by-defect recombination are shown in Fig. 6(c). It is found that the e-h recombination rate of deep level defects is even lower than that of shallow level defects, such as  $R_{\text{nr}(\text{MAPb})} > R_{\text{nr}(\text{Pb}_3)}$ , suggesting that both deep and shallow level defects may lead to e-h non-radiative recombination. Through quantitative e-ph coupling analysis, it is found that due to the soft structure, only low-frequency phonons contribute to the e-h recombination regardless of defects [Fig. 6(d)], and the corresponding non-adiabatic coupling (NAC) is small, which makes e-h non-radiative recombination slow down [Fig. 6(e)]. This is why perovskites can be used as EMLs even though they have many defects.

## E. Self-trapping excitons

Free charge-carriers and free excitons recombination are both intrinsic recombination processes in perovskites. At room temperature, there is a small Stokes shift between the absorption spectrum and the emission spectrum with the narrow spectral range. There is a special case that the local electron states caused by e-ph coupling will produce polarons and STEs, which play a significant role in broad-spectrum luminescence.<sup>102,103</sup> Figure 7(a) shows a schematic of the STEs, in which electrons and holes are quickly self-trapped after light excitation.<sup>104</sup> Here,  $E_{\text{st}}$  refers to the energy loss of excitons during this process, and  $S_{1/2}$  reflects the strength of the e-ph coupling and increases as the strength of the e-ph coupling increases. The larger  $S_{1/2}$  is, the wider the emission spectrum is and the larger the Stokes shift is.

Perovskite materials have a “soft” lattice, strong e-ph coupling and rapid lattice distortion, which leads to self-trapping of electrons and holes, generating local polarons [Fig. 7(b)].<sup>105</sup> According to the intensity of e-ph coupling, it can be divided into large and small polarons. When there are extra electrons in hybrid perovskites, the strong Coulomb interaction between excess carriers and lattice enhances the electron-vibration coupling. In this case, electrons can be delocalized within a few unit cells, forming large polarons similar to free excitons [image A in Fig. 7(b)]. Conversely, if the extra electrons are confined to a volume of about one unit or less, a small polaron is formed. The structures of self-trapped electrons and holes in  $\text{PbBr}_2$  have been verified. Self-trapped electron localizes on a  $\text{Pb}^{2+}$ , and then combines with another  $\text{Pb}^{2+}$  to form a dimer  $\text{Pb}_2^{3+}$ . Correspondingly, self-trapped hole localizes on  $\text{Br}^-$  and then combines with another  $\text{Br}^-$  to form  $\text{Br}_2^-$  [image B and C in Fig. 7(b)].<sup>105</sup> The polaron behavior of

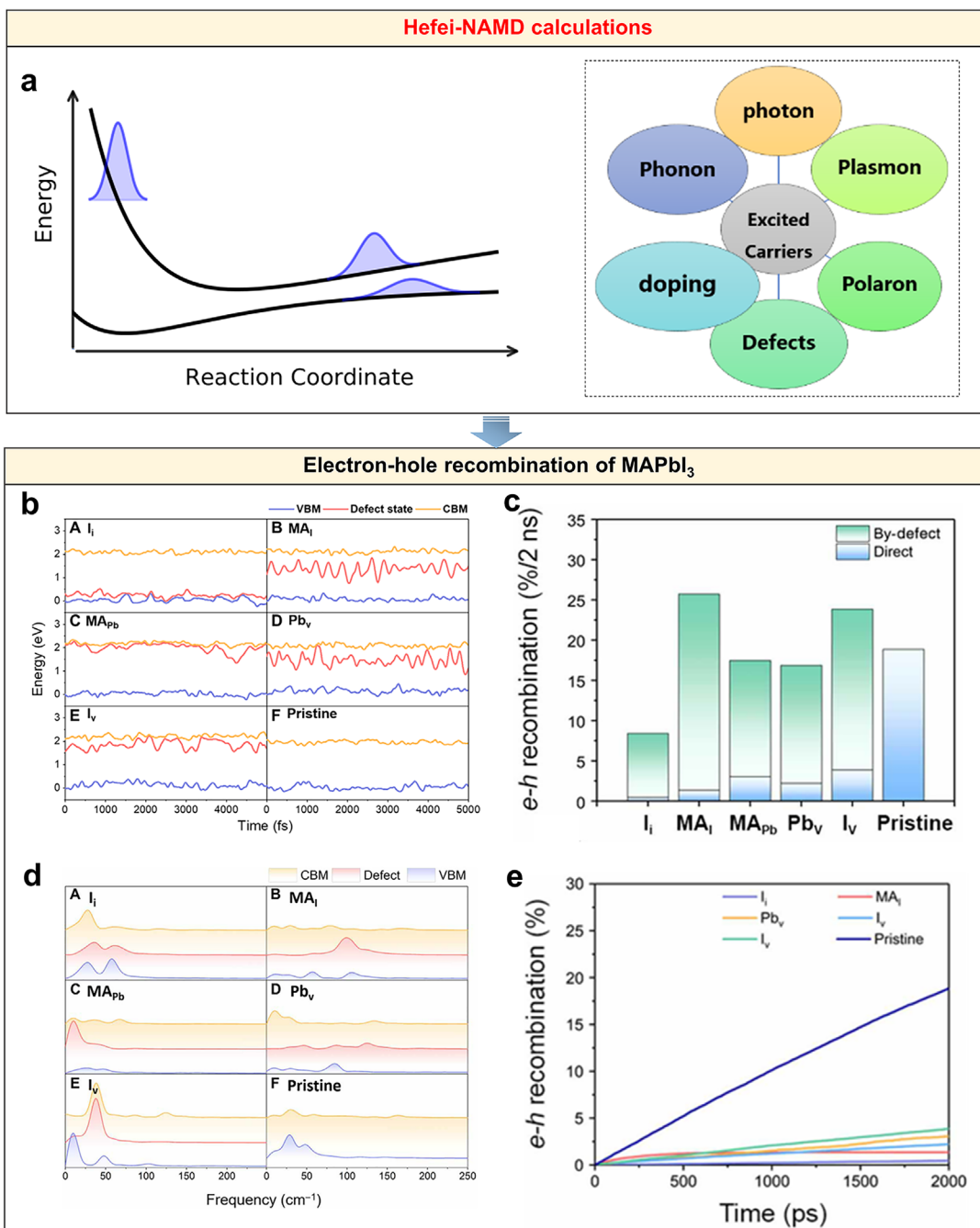


**FIG. 6.** (a) Schematic diagram of Hefei-NAMD. (b) The time evolution of the VBM, CBM and defect state of the  $\text{MAPbI}_3$  at 300 K. (c) The e-h recombination percentage for different systems after 2 ns. (d) The Fourier transform spectra of the VBM, CBM, and the defect state. (e) Time-dependent e-h direct non-radiative recombination percentage. Reproduced with permission from Zhao and Saidi *et al.*, Sci. Adv. **6**, eaaw7453 (2020). Copyright 2020 AAAS.<sup>101</sup>

perovskites has made some progress experimentally and theoretically. For example, Bonn *et al.* found that in  $\text{MAPbI}_3$ ,  $\text{FAPbI}_3$ , and  $\text{CsPbI}_3$ , similar polaron dynamics are observed by using Terahertz time-domain spectroscopy (ThZ-TDS), and polarons can be formed within 400 fs, indicating that polaron formation is independent of cation

type, only related to the formation of inorganic lattice.<sup>106</sup> In many cases, these polaron states are expected to introduce energy levels into the bandgap, which is the cause of luminous emission.<sup>107</sup>

STEs are similar to small polaron, which can be easily observed in perovskites, especially low-dimensional perovskites [Fig. 7(c)].

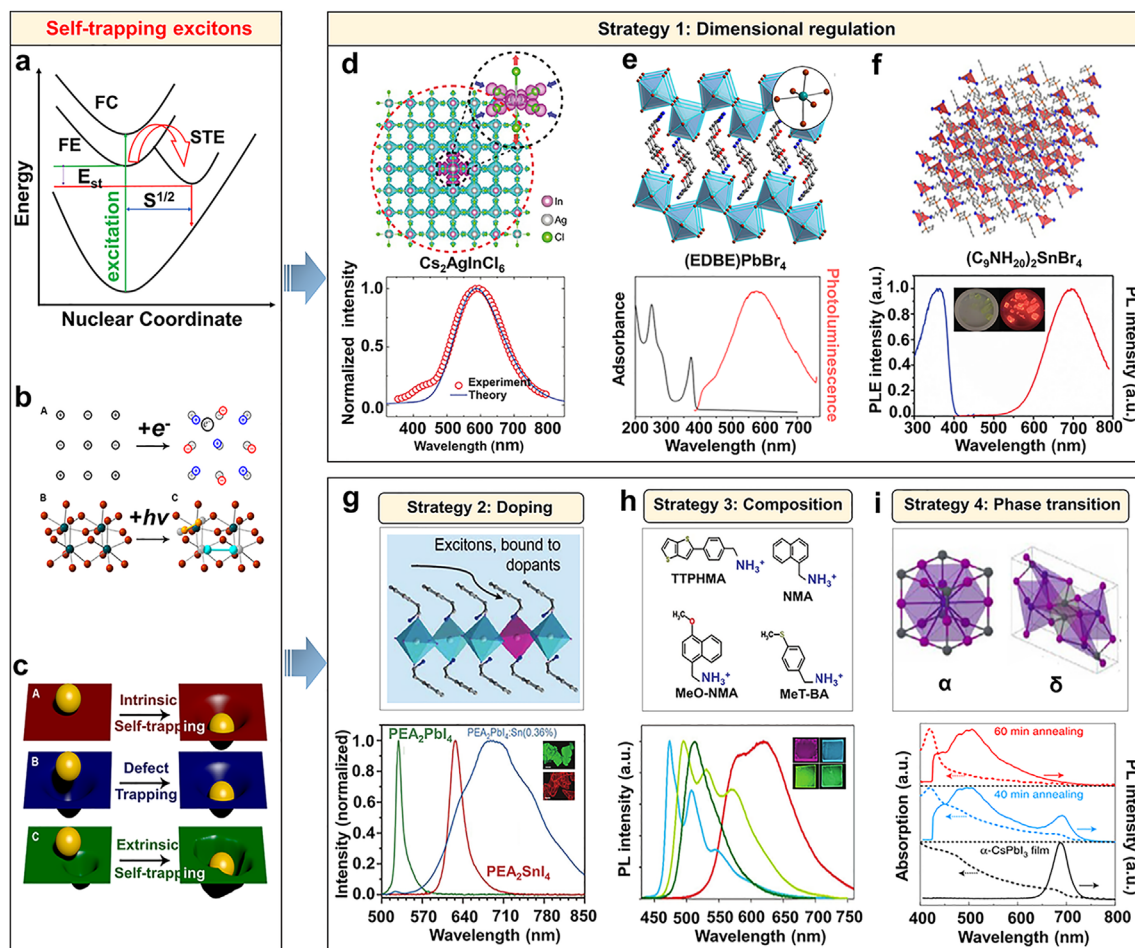


**FIG. 7.** (a) Schematic diagram of forming self-trapping excitons. (b) Schematic diagram of a large polaron formed by adding an electron to a lattice in A; Crystal structure of  $\text{PbBr}_2$ . Green and red spheres represent Pb and Br atoms, respectively, in B; Schematic of the  $\text{Br}_2^-$  (orange balls) and  $\text{Pb}_2^{3+}$  (light blue balls) dimers formed by the self-trapped hole and self-trapped electron, respectively, in C. (c) Self-trapping of intrinsic in A; trapping at permanent defects in B; self-trapping of extrinsic in C. Reproduced with permission from Karunadasa *et al.*, *Acc. Chem. Res.* **51**, 619 (2018). Copyright 2018 American Chemical Society.<sup>105</sup> (d) Structure diagram (upper) and emission spectrum (lower) of double perovskite  $\text{Cs}_2\text{AgInCl}_6$ . Reproduced with permission from Sargent and Tang *et al.*, *Nature* **563**, 541 (2018). Copyright 2018 Nature Publishing Group.<sup>112</sup> (e) Crystal structure (upper) and emission spectra of 2D layered (EDBE) $\text{PbBr}_4$  perovskite. Reproduced with permission from Karunadasa *et al.*, *J. Am. Chem. Soc.* **136**, 13154 (2014). Copyright 2014 American Chemical Society.<sup>113</sup> (f) Crystal structure (upper), crystal photographs, excitation and emission spectra of 0D perovskite  $(\text{C}_9\text{NH}_{20})_2\text{SnBr}_4$  (lower). Reproduced with permission from Ma *et al.*, *Angew. Chem. Int. Ed. Engl.* **57**, 1021 (2018). Copyright 2018 Wiley-VCH.<sup>116</sup> (g) Crystal structure (upper), emission spectra and photoluminescence photographs of  $(\text{PEA})_2\text{PbI}_4$  and  $(\text{PEA})_2\text{PbI}_4\text{Sn}$  (0.36%) (lower). Reproduced with permission from Chen *et al.*, *Adv. Mater.* **31**, 1806385 (2019). Copyright 2019 Wiley-VCH.<sup>118</sup> (h) Schematic diagram of the molecular structure of perovskite organic cation (upper) and emission spectra and photoluminescence photographs with four different organic ligands TTPHMA, MEO-NMA, NMA and MET-BA (lower). Reproduced with permission from Lam *et al.*, *Adv. Mater.* **30**, 1707621 (2018). Copyright 2018 Wiley-VCH.<sup>119</sup> (i) Crystal structure (upper) PL and absorption spectra of  $\alpha$ - $\text{CsPbI}_3$  and  $\delta$ - $\text{CsPbI}_3$  at different wavelengths (lower). Reproduced with permission from Zeng *et al.*, *Nat. Photonics* **15**, 238 (2020). Copyright 2021 Nature Publishing Group.<sup>120</sup>

Specifically, STEs are divided into intrinsic and extrinsic self-trapping. However, it is difficult to distinguish them using spectra at present. Generally, the recombination luminescence characteristics of STEs depend on the specific crystal structure. The larger the distortion of the  $\text{PbX}_6$  octahedron is, the wider the spectral width of the STEs is, which shows a broad spectrum of fluorescence emission, providing a choice for the realization of white light emission in a single emitter layer. In LEDs, a single emitter layer can not only avoid the color imbalance caused by the interaction between different luminescent

materials but also reduce the energy loss and improve the luminous efficiency. Therefore, the luminescent materials with single emitter layer white light emission are of particular interest and become the research hotspot of the new generation of white-light LEDs.<sup>108–110</sup> Since Karunadasa *et al.* discovered that 2D layered perovskites emit white light from a single matrix in 2014,<sup>111</sup> the white light emission of different dimensions of perovskites and double perovskites has been extensively studied. Among them, the double perovskite STEs luminescence is a typical example. In 2018, Tang and his group reported

that  $\text{Cs}_2\text{AgInCl}_6$  has broadband white light emission of STEs, and the PL spectrum covers the whole visible range of 400–800 nm. The PLQY increased to  $(86 \pm 5)\%$  with  $\text{Na}^+$  and Bi doping [Fig. 7(d)].<sup>112</sup> The 2D layered  $(\text{EDBE})\text{PbBr}_4$  ( $\text{EDBE} = 2,2'$ -(ethylenedioxy)bis(ethylammonium) also shows a broad spectrum of emission, covering the entire visible spectrum [Fig. 7(e)].<sup>113</sup> In addition to the above materials, 1D and 0D metal halide luminescent materials have also been studied extensively in STEs luminescence.<sup>114–117</sup> Figure 7(f) shows the 0D perovskite  $(\text{C}_9\text{NH}_{20})_2\text{SnBr}_4$ , which shows a strong Stokes shift ( $\sim 332$  nm) broadband red emission with an emission peak of about 695 nm, half-maximum (FWHM) of 146 nm, and a PLQY of about 46%.<sup>116</sup> In addition to structural dimension, doping, composition and phase transition can also achieve spectral regulation. Chen *et al.* found that undoped  $(\text{PEA})_2\text{PbI}_4$  ( $\text{PEA} = \text{phenylethylammonium}$ ) and  $(\text{PEA})_2\text{SnI}_4$  are emitted only by narrow-band free excitons. When 0.36%  $\text{Sn}^{2+}$  is doped in  $(\text{PEA})_2\text{PbI}_4$ , additional self-trapping wideband red-near infrared (NIR) emission is generated at about 700 nm [Fig. 7(g)].<sup>118</sup> In this STEs luminescence, quantum yield is 8.6 times higher than that without doping. Lam *et al.* selected four different organic ligands thieno [3,2-b]thiophene-2-phenylmethylammonium (TPPHMA), alkoxy side group-NMA (MEO-NMA), naphthalenemethylammonium (NMA) and methylthiobenzene cation (MET-BA) to regulate the luminescence properties. Among them, TPPHMA compound generates a broad-spectrum emission peak at 620 nm. The emission spectra of NMA compounds shows a significant blue shift compared with other systems, and this wide range of spectral adjustment is due to the selection of organic ligands. [Fig. 7(h)].<sup>119</sup> Zeng and his co-workers developed a phase transition synergistic film, which consists of narrow spectral emission of  $\alpha\text{-CsPbI}_3$  phase and wide spectral emission of STEs of  $\delta\text{-CsPbI}_3$  phase [Fig. 7(i)], achieving high-quality broadband white light emission.<sup>120</sup> In addition, halogens also play a significant role in STEs luminescence, in which STEs emission is stronger than free excitons emission for lighter halide compounds ( $\text{Cl} > \text{Br} > \text{I}$ ).<sup>121</sup>

### III. CHARGE-CARRIER DYNAMICS FOR PeLEDs

From the perspective of material optimization, the luminescence properties of perovskites can be improved by decreasing the defect-induced non-radiative recombination and Auger recombination. Back to the formula (1), PLQY can be effectively ameliorated through the analysis and strategies in Sec. II. However, the above-mentioned in Sec. II is based on the premise of carrier injection balance, the injection in PeLEDs is always unbalanced, leading to a difficult equality of PLQY and EQE.<sup>122–127</sup> This requires effective adjustment of the injection factor ( $\eta_{\text{injection}}$ ), which in turn is closely related to the interface, because the carrier injection process will reach EML through many interfaces for PeLEDs. Therefore, it is significant to study interface carrier behavior to obtain high performance PeLEDs.<sup>128</sup> These complex processes shown in Fig. 8(b) include (1) electrons and holes are injected into the electron transport layer (ETL) and hole transport layer (HTL) from the cathode and anode, respectively; (2) electrons and holes are injected into the EML from the transport layers ETL and HTL; (3) and electrons and holes in the EML recombine in the form of free carriers or excitons. Since process (3) has already been discussed in Sec. II, we will focus on some of the known issues of the restriction processes (1) and (2), as well as control techniques to overcome these issues.

### A. Interface in PeLEDs

Generally, PeLEDs, like previous EL devices, can be classified into an inverted and a normal device structure.<sup>130</sup> The device structure that emits photon from the anode is generally called normal type, while from the cathode it is an inverted device. Taking the normal device as an example, it is composed of electrode layers (cathode and anode), EML, and charge-carrier transport layers (ETL and HTL). To limit the charge-carriers of HTL and ETL into the EML, the VBM of HTL is not allowed to be higher than that of the EML; otherwise, there will be a hole injection barrier in process (2). In addition, the CBM should be as high as possible to realize the blocking of electrons.<sup>131</sup> Similarly, the CBM of the ETL should not be lower than that of the EML, and the VBM of the ETL should be as low as possible to prevent the holes, so that the holes injected by the HTL are confined in the EML.<sup>132</sup> Thus, under the applied electric field, holes and electrons are injected from anode and cathode shown in process (1) in Fig. 8(b), and transported to the EML from HTL and ETL illustrated in process (2) in Fig. 8(b). Finally, the mobilities of the electron and hole transport layers should be as large as possible to reduce the loss of process (2). In processes (1) and (2), electrons and holes need to overcome the interface injection barriers between anode/HTL, cathode/ETL, HTL/EML and ETL/EML, respectively.<sup>133</sup> In the injection process, the carrier mobility and the energy level barrier cooperatively control the carrier transport process. Therefore, it is necessary to select the transport layer materials with better matching energy level and mobility for PeLEDs that enable the electrons and holes to reach the EML simultaneously. Figures 8(c) and 8(d) summarize the energy levels of HTLs, ETLs and EMLs, and mobilities of HTLs, ETLs commonly used in PeLEDs.<sup>129</sup>

### B. Carrier injection balance in PeLEDs

In PeLEDs, interfacial charge-carrier transfer from electrodes to ETL, HTL and then to EML is significant for efficient radiative emission. Thus, the injection efficiency of charge-carriers has attracted much attention due to their critical role in PeLEDs.<sup>134–139</sup> Experiments and theoretical calculations have proved that electron injection is faster than hole injection.<sup>140,141</sup> For example, as can be seen in Fig. 9(a), electrons can be easily injected into the EML and even accumulate in large quantities at the HTL/EML interface due to the excellent electron blocking nature of HTL. However, holes have two injection barriers  $\varphi_1$  (anode/HTL) and  $\varphi_2$  (HTL/EML), which causes hole accumulation at these two interfaces.<sup>142</sup> In addition, if the mobility of HTL is poor, most holes will remain in the HTL and prevent holes being injected into the EML, resulting in the charge-carrier loss. This unbalanced charge-carrier injection is a key factor limiting the high efficiency of devices. Thus, interface engineering and energy level regulation are effective methods to improve hole injection and reduce the accumulation of HTL/EML interface carriers.<sup>133</sup>

An effective approach is to introduce HTL with low VBM. As shown in Fig. 9(b), the adjustment of  $\varphi_2$  to a lower height can be achieved by reducing the VBM of the HTL, thus further reducing the accumulation of HTL/EML, even though the barrier in  $\varphi_1$  is high. As we know, the influence of  $\varphi_2$  in the EQE loss is significantly larger than that of  $\varphi_1$ .<sup>142</sup> Therefore, HTL with deep VBM are used for high performance PeLEDs.<sup>143–145</sup> The most commonly used HTL is poly real (3, 4 ethylenedioxythiophene): poly real-(styrenesulfonate)

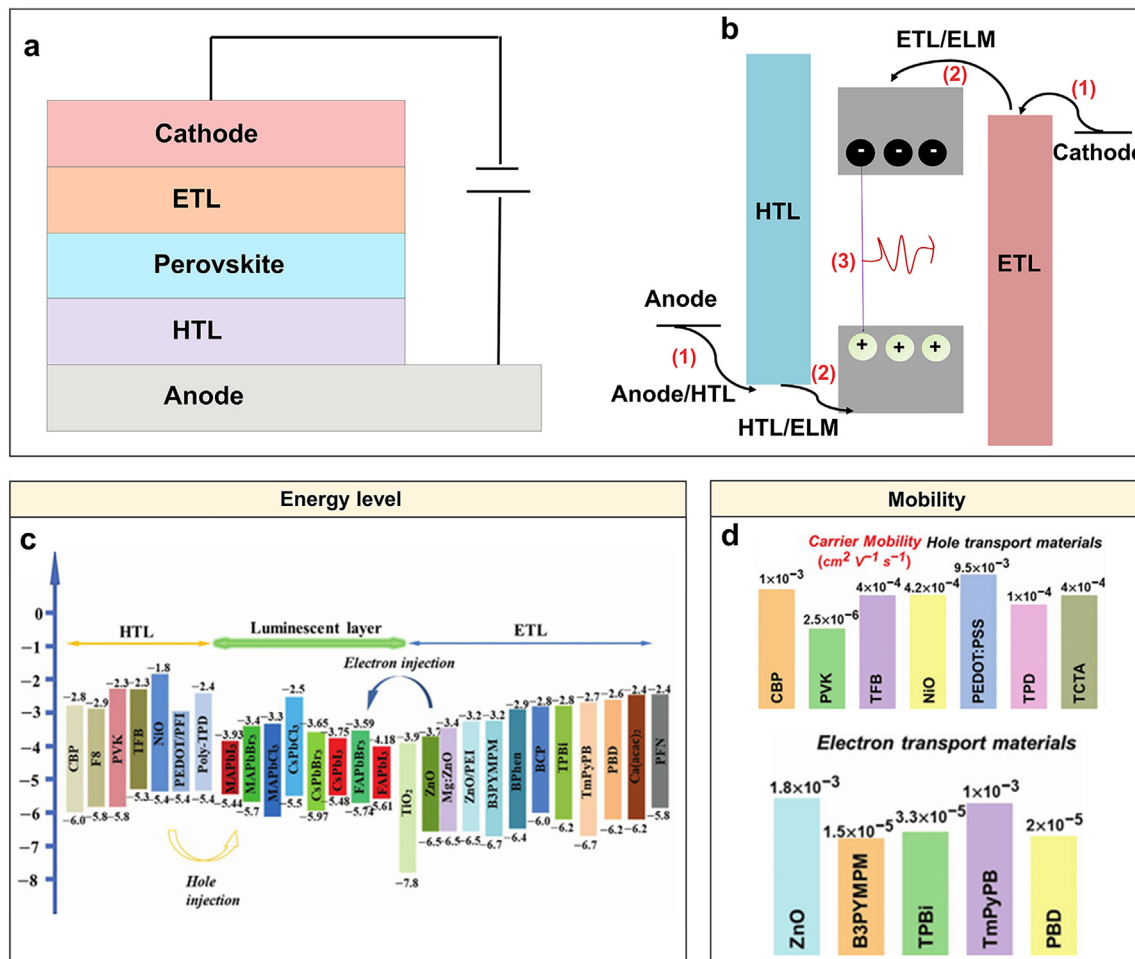


**FIG. 8.** (a) The normal LED structures. (b) Charge-carrier recombination processes include (1) electrons and holes are injected into the charge transport layers ETL and HTL from the cathode and anode, respectively. (2) Electrons and holes are injected into the EML from the transport layers ETL and HTL. (3) Charge-carrier recombination. (c) Commonly used energy levels of HTLs, ETLs, and EMLs. (d) Commonly used mobilities of HTLs and ETLs. Reproduced with permission from Tian *et al.*, *Adv. Opt. Mater.* **9**, 2002167 (2021). Copyright 2021 Wiley-VCH.

(PEDOT:PSS) due to its high carrier mobility, which facilitates hole injection.<sup>146</sup> However, the VBM of PEDOT:PSS ( $-4.9 \text{ eV}$ ) is not sufficient to match the VBM of  $\text{CsPbBr}_3$  at  $-5.97 \text{ eV}$  and the VBM of  $\text{MAPbBr}_3$  at  $-5.7 \text{ eV}$ , etc., thus limiting hole injection.<sup>142,147</sup> An appropriate energy level structures can be achieved by introducing a thin interface layer, such as tetrafluoroethylene-perfluorooctane-3,6-dioxa-4-methyl-7-octene-sulfonic acid copolymer (PFI),<sup>51,147</sup> polyethylenimine (PEI),<sup>132</sup> and polyethylenimine ethoxylated (PEIE).<sup>148</sup> Lee *et al.* modified HTL by adding PFI to increase its (PEDOT:PSS is abbreviated as Buf-HIL) VBM to  $-5.95 \text{ eV}$ , which reduced the hole injection barrier at HTL/ $\text{CH}_3\text{NH}_3\text{PbBr}_3$  interface and increased the hole injection, leading to a more balanced charge-carriers injection [Figs. 10(a) and 10(b)].<sup>147</sup> Subsequently, Rogach *et al.* also added PFI between the HTL and EML, resulting in an increasing of  $0.34 \text{ eV}$  of VBM, making hole injection easier.<sup>131</sup> Some other materials, such as sodium-poly(styrenesulfonate) (S-PSS), poly(4-styrenesulfonic acid) (PSSA),  $\text{MoO}_3$ , etc., are also used to doping PEDOT:PSS to improve the hole

injection power.<sup>149–151</sup> In addition, inorganic materials are also a good choice due to their insensitivity to water and oxygen.<sup>152–157</sup> For example, Song *et al.* discovered that the VBM of PEDOT:PSS and  $\text{NiO}_x$  is  $-5.15$  and  $-5.18 \text{ eV}$ , respectively, and calculated energy barriers are  $0.3$  (PEDOT:PSS/EML) and  $0.17 \text{ eV}$  ( $\text{NiO}_x$ /EML), as shown in Fig. 10(c). This result means that  $\text{NiO}_x$  shows a better hole injection characteristics when it is used in PeLEDs. Compared with PEDOT:PSS, PeLEDs prepared by  $\text{NiO}_x$  show significant operational stability [Fig. 10(d)].<sup>158</sup> Subsequently, in 2020, Jin *et al.* proposed a simple self-assembled molecular layer surface modification strategy and selected 4-(trifluoromethyl)benzoic acid ( $\text{BA-CF}_3$ ) to modify the original  $\text{NiO}_x$  film, achieving a  $\text{NiO}_x$  film with a highly stable work function (WF) of about  $5.7 \text{ eV}$  [Fig. 10(e)]. This change in the work function is due to the shift of the vacuum energy level caused by the interface dipole [Fig. 10(f)]. At an initial brightness of  $1000 \text{ cd m}^{-2}$ , the device had a  $T_{95}$  lifetime of about  $2500 \text{ h}$ , which met the commercial requirements for display applications.<sup>159</sup> As mentioned above, a relatively large  $\phi_1$  at

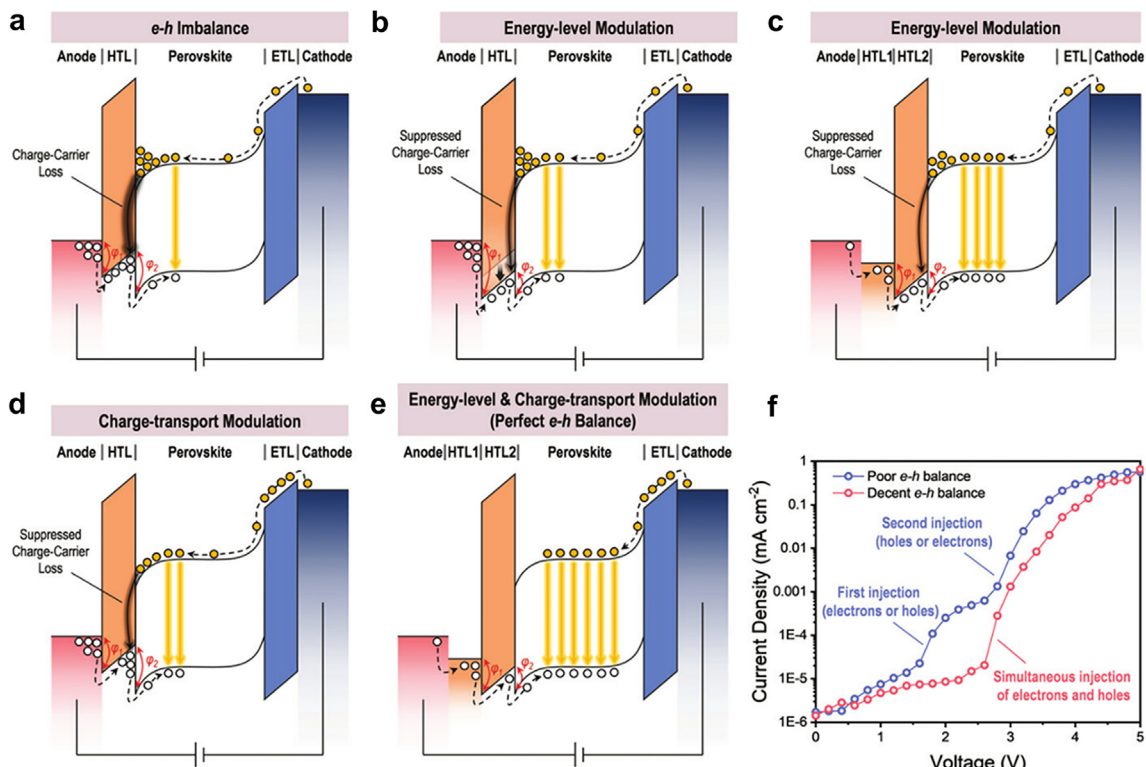


**FIG. 9.** Strategies to achieve balance of electrons and holes injection. (a) Schematic diagram of electrons and holes injection imbalance. (b) Reducing  $\varphi_2$  barrier by adding a deep VBM of HTL. (c) Double HTLs to increase hole injection. (d) Charge-carrier transfer mechanism of ETL and HTL. (e) Schematic diagram of the perfect injection balance of electrons and holes. (f) I-V curves with inferior and decent e-h injection balance in PeLEDs. Reproduced with permission from Yip *et al.*, Rep. Prog. Phys. **84**, 046401 (2021). Copyright 2021 IOP Publishing Ltd.<sup>142</sup>

the anode/HTL interface results in significant holes accumulation when a deep VBM material is used as the HTL, but hole injection can be increased when another HTL with a medium energy level is introduced to form a double HTL (HTL1|HTL2), as shown in Fig. 9(c). Here, HTL1 is generally a material with a high hole mobility, such as PEDOT: PSS ( $\sim 9.5 \times 10^{-3} \text{ cm}^2 \text{ V}^{-1} \text{ s}^{-1}$ ), TFB ( $\sim 4 \times 10^{-4} \text{ cm}^2 \text{ V}^{-1} \text{ s}^{-1}$ ) and NiO<sub>x</sub> ( $\sim 4.2 \times 10^{-4} \text{ cm}^2 \text{ V}^{-1} \text{ s}^{-1}$ ). HTL2 generally has a deeper VBM, such as poly(9-vinylcarbazole) (PVK,  $-5.8 \text{ eV}$ ), poly(9,9-diptylfluorene-co-N-(4-(3-methylpropyl)) diphenylamine) (TFB,  $-5.3 \text{ eV}$ ) and poly(4-butylphenyl-diphenylamine) (poly-TPD,  $-5.4 \text{ eV}$ ). Such dual HTLs always contribute to improve the performance of PeLEDs.<sup>13,54,131,160–162</sup>

In addition to increasing hole injection, reducing electron injection is also a strategy, which inhibits charge-carrier accumulation at HTL/EML interface, as shown in Fig. 9(d). For the ETLs, thin insulating layers are often inserted between ETLs and the EMLs to reduce electron injection.<sup>163,164</sup> For instance, Wei *et al.* proposed a CsPbBr<sub>3</sub> at MABr half-core shell structure, in which a poly(methyl methacrylate) (PMMA) insulating layer is inserted into ETL and EML to reduce electron injection, improve charge-carrier injection balance, and increase EQE to more than 20% with a half-lifetime over 100 h at 100 cd m<sup>-2</sup>.<sup>14</sup> Yang *et al.* introduced lithium fluoride (LiF) between the ETL/EML interface, which not only promoted the charge-carrier balance but also passivated the defects in the EML and inhibited the fluorescence

quenching, thereby leading to a high EQE of 16.35% [Fig. 10(g)].<sup>165</sup> Recently, Song and his team applied a double ETL to balance the charge-carrier injection in green light perovskite quantum dot light-emitting diode, and the EQE is as high as 21.63%, as shown in Figs. 10(h) and 10(i), which is one of the most efficient QLED at present.<sup>166</sup> Meanwhile, due to the reduction of charge-carrier accumulation effect, the quenching of the EML is effectively avoided, and the half-lifetime of the PeLED is significantly improved, which exceeds 180.1 h at the brightness of 100 cd m<sup>-2</sup>. If both electrons and holes can reach EML at the same time, perfect e-h radiative recombination can be achieved without any carrier loss at the interface, as shown in Fig. 9(e). Unfortunately, this is very difficult to achieve the excellent carrier injection balance. The current density–voltage curves in Fig. 9(f) show that two turning points occur in devices with poor e-h injection balance, which may be responsible for the imbalance of carrier injection. For devices with relatively decent e-h injection balance, only a jump in current density is observed, indicating that both electrons and holes are injected into EML simultaneously.

### C. Characterization and simulation techniques of charge-carrier dynamics in PeLEDs

The behavior of charge-carrier dynamics in materials and devices, such as transport, injection and recombination, is the key to study

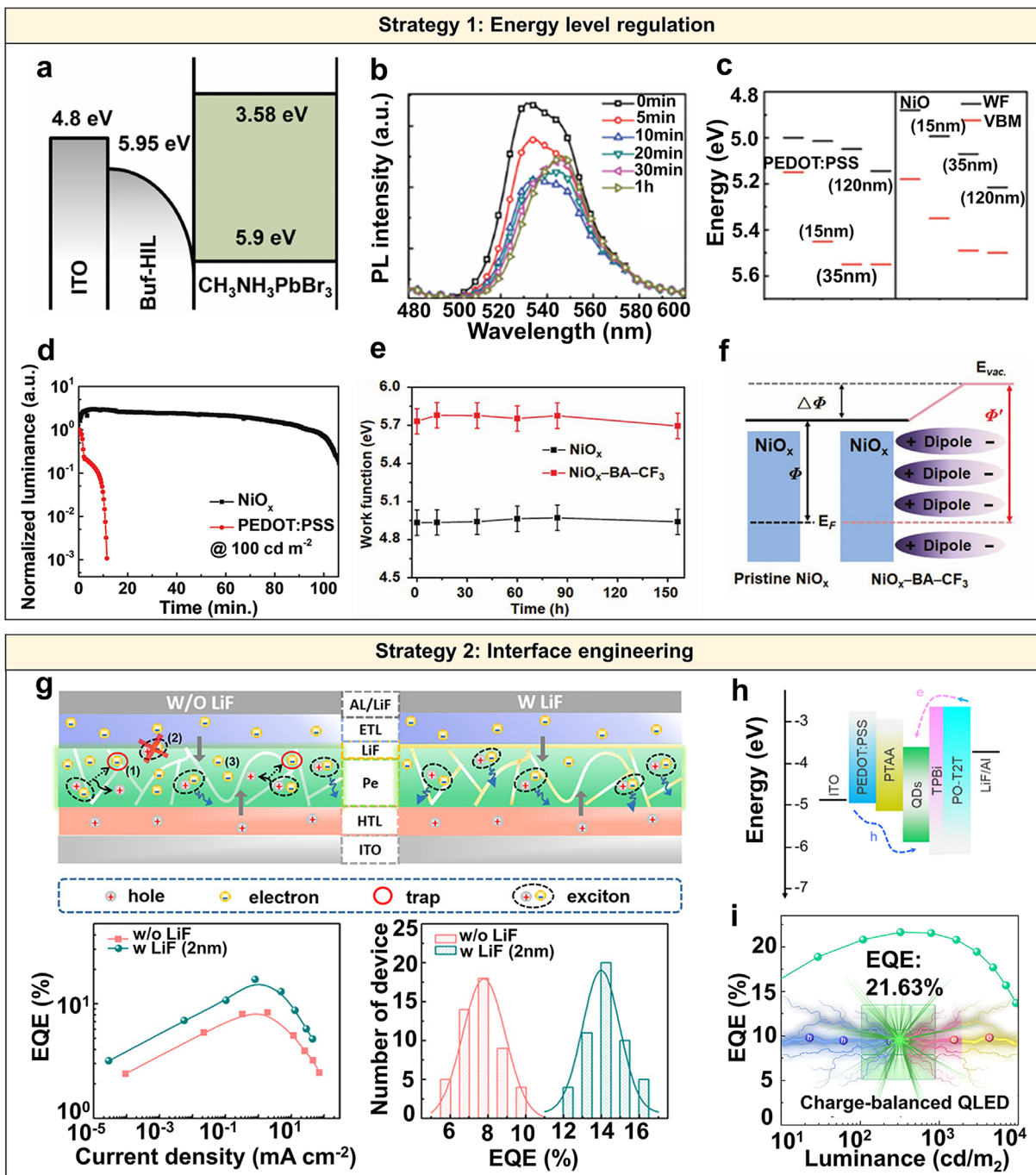


**FIG. 10.** (a) Energy level diagram of anode/Buf-HIL/CH<sub>3</sub>NH<sub>3</sub>PbBr<sub>3</sub>. (b) PL spectra at different time periods. Reproduced with permission from Lee *et al.*, *Adv. Mater.* **27**, 1248 (2014). Copyright 2014 WILEY-VCH.<sup>147</sup> (c) Work function (WF) and VBM for pristine NiO<sub>x</sub> and PEDOT:PSS, as well as perovskite films of 15, 35, and 120 nm deposited on NiO<sub>x</sub> and PEDOT:PSS. (d) Normalized luminance of PeLED prepared by  $n = 3$  quasi-2D perovskite deposited on NiO<sub>x</sub> and PEDOT:PSS as a function of operating time. Reproduced with permission from Song *et al.*, *Adv. Sci. (Weinh)* **5**, 1801350 (2018). Copyright 2018 Wiley-VCH.<sup>158</sup> (e) Work functions of NiO<sub>x</sub> and NiO<sub>x</sub>-BA-CF<sub>3</sub> as a function of time. (f) Schematic diagram of dipole-induced changes in the work function of NiO<sub>x</sub>. Reproduced with permission from Jin *et al.*, *Adv. Funct. Mater.* **30**, 1907265 (2019). Copyright 2019 Wiley-VCH.<sup>159</sup> (g) Schematic diagram of interface dynamics with or without lithium fluoride (LiF). The function between EQE and current density with or without LiF (lower left corner). Schematic diagram of peak EQE of 50 devices under the same manufacturing conditions (lower right corner). Reproduced with permission from Yang *et al.*, *ACS Appl. Mater. Interfaces* **12**, 43018 (2020). Copyright 2020 American Chemical Society.<sup>165</sup> (h) Energy level diagram of QLED. (i) The EQE of charge-balanced QLED is up to 21.63%. Reproduced with permission from Song *et al.*, *Sci. Bull.* **66**, 36 (2021). Copyright 2021 Elsevier BV.<sup>166</sup>

the luminescence mechanism and also an important basis to guide the improvement of PeLEDs. Parameters that express these behaviors are mobility, defect density, and recombination efficiency, which can be characterized by optical, electrical and simulation techniques.

### 1. Mobility characterization techniques

Mobility, a key indicator of charge-carrier transport capacity, is commonly characterized by electronic probes, such as transient EL (Tr-EL),<sup>167</sup> space charge limited current (SCLC),<sup>168</sup> time-of-flight (TOF),<sup>169–171</sup> and optical probe measurement, such as time-resolved microwave conductivity (TRMC),<sup>172–174</sup> and optical-pump/THz-probe.<sup>175,176</sup> It is significant to understand these techniques before using them to accurately measure the mobility of perovskites, and then the researcher can choose the appropriate techniques depending on the state of the sample and the needs of the testing method.

In electrical probe measurements, when the carrier mobility is measured by Tr-EL, a rectangular pulse voltage is applied to the device to generate a time-dependent electroluminescence signal. There is a delay time between the start time of the device and the pulse voltage, that is, the transient electroluminescence time. Wang *et al.* studied the MQW-based PeLEDs by using Tr-EL, as exhibited in Fig. 11(a).<sup>167</sup>

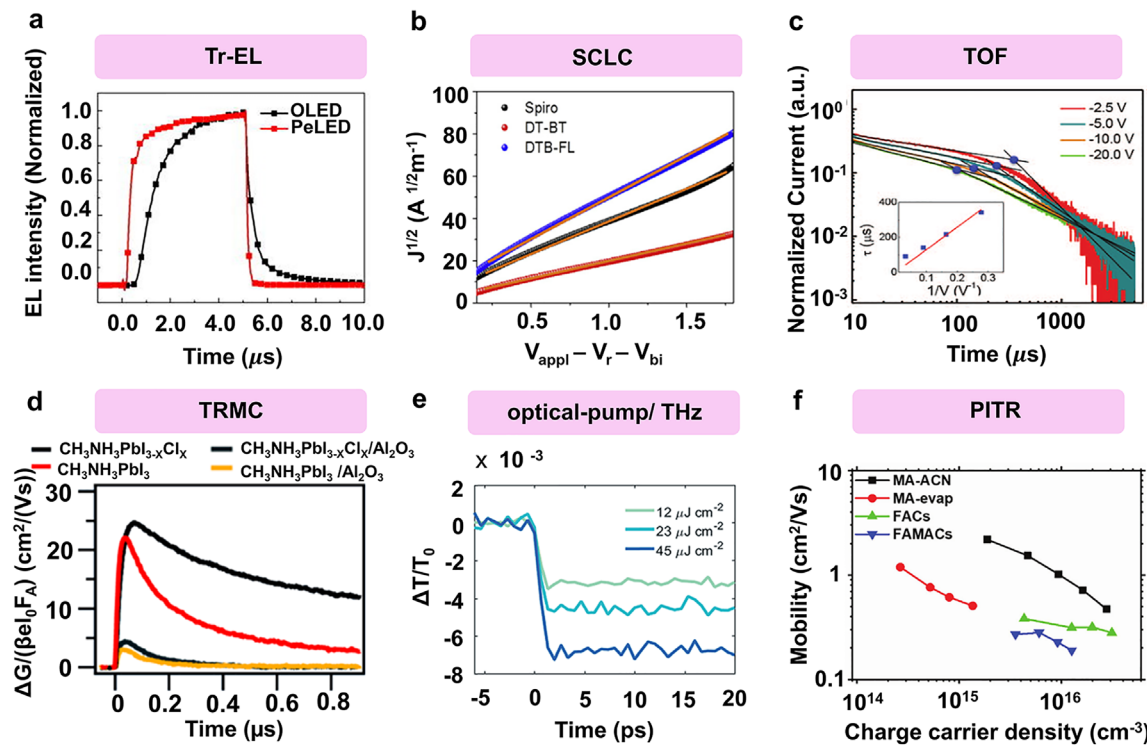


**FIG. 11.** (a) The Tr-EL of OLED and PeLED at the 5 V. Reproduced with permission from Wang *et al.*, *Appl. Phys. Lett.* **115**, 041102 (2019). Copyright 2019 American Institute of Physics Publishing.<sup>167</sup> (b) SCLC method is used to test hole mobility of different materials. Reproduced with permission from Cao *et al.*, *Joule* **5**, 249 (2021). Copyright 2021 Elsevier.<sup>177</sup> (c) TOF method characterizes electron mobility. Inset shows the relationship between charge transfer time and reciprocal bias. Reproduced with permission from Huang *et al.*, *Science* **347**, 967 (2015). Copyright 2015 AAAS.<sup>179</sup> (d) The mobility of  $\text{CH}_3\text{NH}_3\text{PbI}_{3-x}\text{Cl}_x$ ,  $\text{CH}_3\text{NH}_3\text{PbI}_3$ , and  $\text{CH}_3\text{NH}_3\text{PbI}_{3-x}\text{Cl}_x/\text{Al}_2\text{O}_3$ ,  $\text{CH}_3\text{NH}_3\text{PbI}_3/\text{Al}_2\text{O}_3$  are measured by TRMC. Reproduced with permission from Savenije *et al.*, *J. Phys. Chem. Lett.* **6**, 3082 (2015). Copyright 2015 American Chemical Society.<sup>180</sup> (e)  $\Delta T/T_0$  of 75% M(MAPI) and 25% T(tBAPI) measured by optical pump/terahertz probe (THz). Reproduced with permission from Correa-Baena *et al.*, *J. Mater. Chem. A* **7**, 23949 (2019). Copyright 2019 The Royal Society of Chemistry.<sup>30</sup> (f) The mobility of different materials is determined by PITR. Reproduced with permission from Snaith *et al.*, *Energy Environ. Sci.* **12**, 169 (2019). Copyright 2019 The Royal Society of Chemistry.<sup>4</sup>

MQW perovskite films are prepared from NMAI (1-naphthylmethylamine iodide), FAI (formamidinium iodide), and  $\text{PbI}_2$  precursor solutions with a molar ratio of 2:1:2 in DMF (N, N-dimethyl formamide). The results indicate that onset time of PeLED is very short  $\sim 0.1 \mu\text{s}$  and the rising time is  $0.15 \mu\text{s}$ , which is much shorter than that of OLED [the structure is: ITO/N,N'-di-1-naphthyl-N,N'-diphenylbenzidine (NPB, 30 nm)/tri-(8-hydroxyquinoline)-aluminum ( $\text{Alq}_3$ , 40 nm)/LiF(1 nm)/Al], indicating that the carrier mobility of MQW perovskites is higher than  $\text{Alq}_3$ . The electron mobility in the perovskites is estimated at  $10^{-5} \text{ cm}^2 \text{ V}^{-1} \text{ s}^{-1}$ , which is consistent with the results obtained by SCLC method. SCLC technique is one of the simplest steady-state contact methods to be used for the determination of electron and hole mobility in perovskites. Ye's group measured the mobility of three different hole-transport materials, including TPAOMe-BT-Br, DT-BT and DTB-FL by using SCLC method, and found that undoped TDB-FL presented excellent charge-carrier mobility of  $3.94 \times 10^{-3} \text{ cm}^2 \text{ V}^{-1} \text{ s}^{-1}$  at 200 nm film thickness [Fig. 11(b)].<sup>177</sup> The main challenge with SCLC is that it can accurately measure the mobility of films with low intrinsic charge-carrier density of  $10^{14} \text{ cm}^{-3}$ , while the charge-carrier density of perovskite films is  $10^{15}$  to  $10^{17} \text{ cm}^{-3}$ .<sup>171</sup> TOF is another electrical contact probe method. When a deflection voltage is applied in the device and the laser is turned on, the laser excites the materials to produce

photogenerated carriers, which move in a directional manner under the action of an electric field. Then, the drift current is recorded vs time, and the carrier mobility is finally calculated.<sup>178</sup> Huang *et al.* used TOF to verify the high electron mobilities of  $24.0 \pm 6.8 \text{ cm}^2 \text{ V}^{-1} \text{ s}^{-1}$  in MAPbI<sub>3</sub> single crystals [Fig. 11(c)].<sup>179</sup> However, one of the major challenges in measuring mobility by TOF is the need for light, and the film thickness must be greater than 500 nm to allow the charge-carrier to move laterally through the depletion zone.

In optical probe measurements, TRMC is a contact-free method to measure carrier mobility, which is calculated by detecting the change of sample conductivity. Hutter *et al.* measured the mobility of thin planar films of  $\text{CH}_3\text{NH}_3\text{PbI}_{3-x}\text{Cl}_x$ ,  $\text{CH}_3\text{NH}_3\text{PbI}_3$ , and their meso-structured analogues  $\text{CH}_3\text{NH}_3\text{PbI}_{3-x}\text{Cl}_x/\text{Al}_2\text{O}_3$ ,  $\text{CH}_3\text{NH}_3\text{PbI}_3/\text{Al}_2\text{O}_3$  by using TRMC, which is close to  $30 \text{ cm}^2 \text{ V}^{-1} \text{ s}^{-1}$  [Fig. 11(d)].<sup>180</sup> However, the laser used in TRMC measurement is generally limited to x-ray band, which has a narrow frequency range and a limited detection range. Moreover, this method is not suitable for measuring devices with electrodes. Optical-pump/THz-probe is a non-contact light detection method, which can evaluate the photoconductivity of samples and then obtain the mobility. Correa-Baena *et al.* obtained the result of  $\Delta T/T_0$  using optical-pump/THz-probe, as shown in Fig. 11(e).<sup>30</sup> The photoconductivity can be obtained by the formula  $-\frac{\Delta T}{T_0} = \frac{z_0 d}{1 + N_{\text{quartz}}} \Delta \sigma$ , in which  $\Delta T$  is the change in the THz transmission amplitude,  $T_0$  is the initial THz transmission,  $Z_0 = 377 \Omega$  is the

impedance of air,  $d$  is the photoexcited depth taken as the inverse of absorption coefficient, and  $N_{\text{quartz}}$  is the index of refraction of the quartz substrate at THz frequencies.<sup>181</sup> Then, the mobility can be calculated by the formula  $\Delta \sigma = q \Delta n \mu$ .<sup>182</sup> Snaith's research group demonstrated for the first time a new technology to measure the charge-carrier mobility by using the combination of electric and optical probes. The results show that the transverse mobility of MAPbI<sub>3</sub> polycrystalline perovskite films prepared by acetonitrile/methylamine solvent system is  $\sim 2 \text{ cm}^2 \text{ V}^{-1} \text{ s}^{-1}$  [Fig. 11(f)].<sup>4</sup>

## 2. Defect density characterization technology

Defect density is a key factor in the charge-carrier transport process, which will affect the charge-carrier lifetime and recombination efficiency. Defect density can be characterized by Tr-EL<sup>167</sup> and electrochemical impedance spectroscopy (EI),<sup>183,184</sup> and broadband transient reflectance spectroscopy (TR),<sup>185,186</sup> while time resolved photoluminescence spectra (TRPL)<sup>187–189</sup> and microwave photo-conductivity decay ( $\mu$ PCD)<sup>190</sup> can be used for charge-carrier lifetime measurement.

Tr-EL, as mentioned above, can be used not only to obtain the mobility but also to characterize the defect density. We can see from Fig. 11(a) that when the voltage is turned off, Tr-EL decays much faster than OLED, indicating that the trap density in MQW perovskite

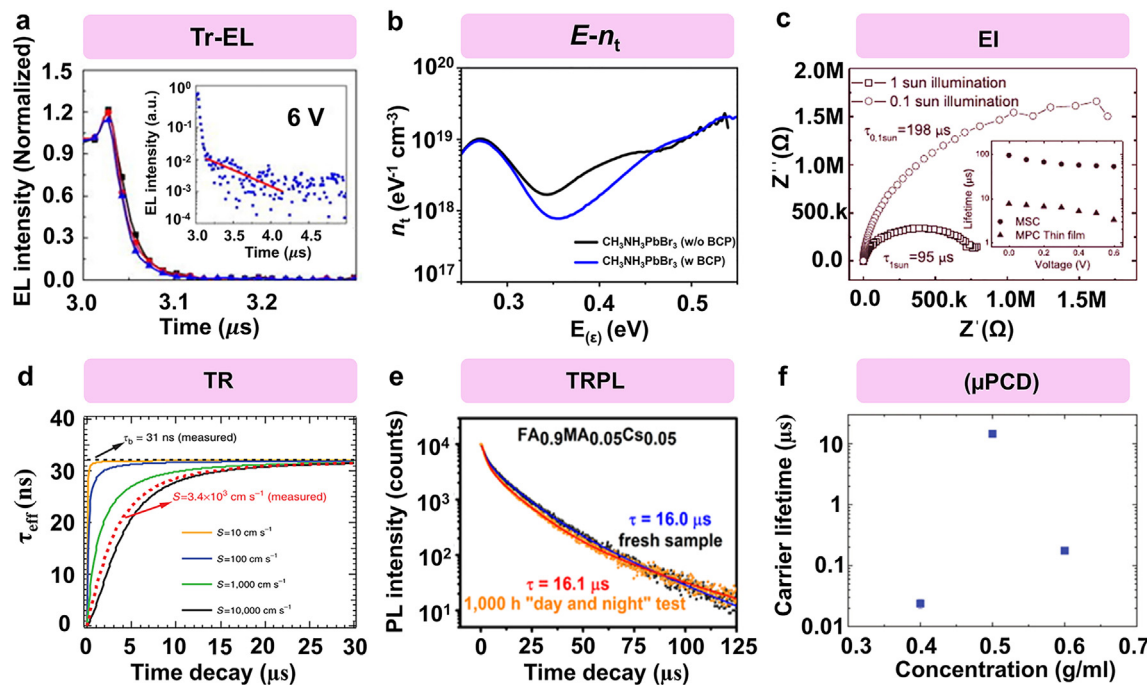


**FIG. 12.** (a) Schematic diagram of function relation between EL and time. Reproduced with permission from Wang *et al.*, Appl. Phys. Lett. **115**, 041102 (2019). Copyright 2019 American Institute of Physics Publishing.<sup>167</sup> (b) Diagram of trap density  $n_T$  as a function of energy  $E$  with or without BCP for PeLED. Reproduced with permission from Hu *et al.*, ACS Appl. Energy Mater. **1**, 6992 (2018). Copyright 2018 American Chemical Society.<sup>191</sup> (c) Impedance spectra of MAPbI<sub>3</sub> of single crystal (MSC) and poly-crystalline (MPC) in 1 and 0.1 sun illumination, respectively. Reproduced with permission from Huang *et al.*, Science **347**, 967 (2015). Copyright 2015 AAAS.<sup>179</sup> (d) Effective lifetime ( $\tau_{\text{eff}}$ ) in polycrystalline films. Reproduced with permission from Beard *et al.*, Nat. Commun. **6**, 7961 (2015). Copyright 2015 Nature Publishing Group.<sup>193</sup> (e) Transient photoluminescence of  $(\text{FAPbI}_3)_{0.9}(\text{MAPbBr}_3)_{0.05}(\text{CsPbBr}_3)_{0.05}$  in 1000 h "day and night" light stability test. Reproduced with permission from Tian *et al.*, J. Am. Chem. Soc. **141**, 1665 (2019). Copyright 2019 American Chemical Society.<sup>188</sup> (f) Average effective carrier lifetimes at the injection level of  $2.5 \times 10^{13} \text{ cm}^{-3}$  for all perovskites. Reproduced with permission from Usami *et al.*, J. Mater. Chem. C **8**, 14481 (2020). Copyright 2020 The Royal Society of Chemistry.<sup>190</sup>

is lower than that in OLED. This result is further revealed in Fig. 12(a), where the electroluminescence decays to zero over a very short time scale ( $0.1 \mu\text{s}$ ), indicating a relatively low trap density for MQW perovskites. The number of charge-carriers is obtained by integrating EL (during the slow-decay period) with time, and then the trap density ( $10^{15} \text{ cm}^{-3}$ ) is roughly obtained, which is similar to the previous data.<sup>32</sup> The defect density can also be obtained according to EI measurement, as shown in Fig. 12(b).<sup>191</sup> The defect density ( $n_t$ ) can be calculated by the following formula:

$$n_t = -\frac{V_{bi}}{q w_0} \frac{dC}{dw} \frac{w}{k_B T}, \quad (7)$$

where,  $V_{bi}$  is the built-in electric field,  $w$  is the angular frequency,  $q$  is the basic charge,  $w_0$  is the depletion zone width,  $k_B$  is the Boltzmann constant, and  $T$  is the temperature.<sup>192</sup> According to the calculations, PeLED with bathocuproine (BCP) has a significantly lower defect density than that of without BCP.

Moreover, the lifetime reflects the number of defects. Therefore, some lifetime characterization techniques play an important role in guiding the optimization of materials and devices. EI is a perturbation technique that can test the lifetime of a sample under nearly reversible conditions. The impedance measurement method is based on the electrochemical response of the samples resulting from the electric field varying with frequency. At steady state, the AC voltage input to the sample can cause perturbations, which can cause changes in the current. The impedance response in the frequency range is given by the relationship between the input AC voltage and the generated response current. Charge-carrier lifetime in  $\text{MAPbI}_3$  single crystal (MSC) at different light intensity is measured using EI, as shown in Fig. 12(c).<sup>179</sup> At 1 sun, the  $\tau$  is  $95 \pm 8 \mu\text{s}$  and, more than 10 times the  $\tau$  value in the best thin-film devices. As for TR method, which reflects recombination dynamics by detecting the changes of photoinduced reflection on the sample surface, there have been some successful examples. For example, Beard *et al.* measured surface recombination dynamics in  $\text{CH}_3\text{NH}_3\text{PbBr}_3$  single crystal at different ultra-low surface recombination velocity

( $S = 10\text{--}10000 \text{ cm s}^{-1}$ ) by using TR, as shown in Fig. 12(d).<sup>193</sup> The effective lifetime is indicated by the red dotted line in the figure. The efficiency increases tenfold as the particle size increases from 1 to  $20 \mu\text{m}$ , and the slope of efficiency growth slows when the particle size is larger than  $20 \mu\text{m}$ . Time resolved photoluminescence spectra (TRPL) is one of the most effective means to characterize the excited state lifetime of perovskites. The test principle is that a pulsed light source injects minority carriers into the sample, and the transient near the emission region can be measured by photomultiplier tube. Mao *et al.* prepared a series of cesium-containing mixed cations and mixed halogen perovskite single crystal. When the cesium content is increased to 10% and/or the bromine content is increased to 15%, a new highly stable compound ( $\text{FAPbI}_3$ )<sub>0.9</sub>( $\text{MAPbBr}_3$ )<sub>0.05</sub>( $\text{CsPbBr}_3$ )<sub>0.05</sub> is developed with a charge-carrier lifetime of  $16 \mu\text{s}$ . It can remain stable in water oxygen test and light stability test at least 10 000 h [Fig. 12(e)].<sup>188</sup> The  $\mu\text{PCD}$  is a contact-free detection method, which is mainly used to monitor the charge-carrier recombination in materials. The  $\mu\text{PCD}$  method is performed at room temperature and free charge-carriers are generated by bandgap optical pulse light injection. After the pulsed light source is stopped, the surface microwave reflection will further measure the conductivity of the sample with time, thus obtaining the carrier lifetime. Recently, the measurement of carrier lifetime mapping is carried out through  $\mu\text{PCD}$  with a wavelength of 394 nm, frequency of 26 GHz and injection level of  $2.5 \times 10^{-13} \text{ cm}^{-3}$ , as shown in Fig. 12(f). When the concentration of  $\text{PbI}_2$  is 0.5 (g/ml), the effective carrier lifetime is the highest, which is  $14.1 \mu\text{s}$ .<sup>190</sup>

### 3. Recombination process characterization techniques

In addition to the characterization of the exact physical parameters, there is also a characterization for the entire charge-carrier dynamic process. It can reflect the process of carrier injection and the exciton recombination efficiency in the devices, which is of significance to the research of carrier injection balance and the improvement of luminescence performance. Capacitance–voltage (C–V) test can describe the carrier recombination characteristics.<sup>194</sup> As can be seen

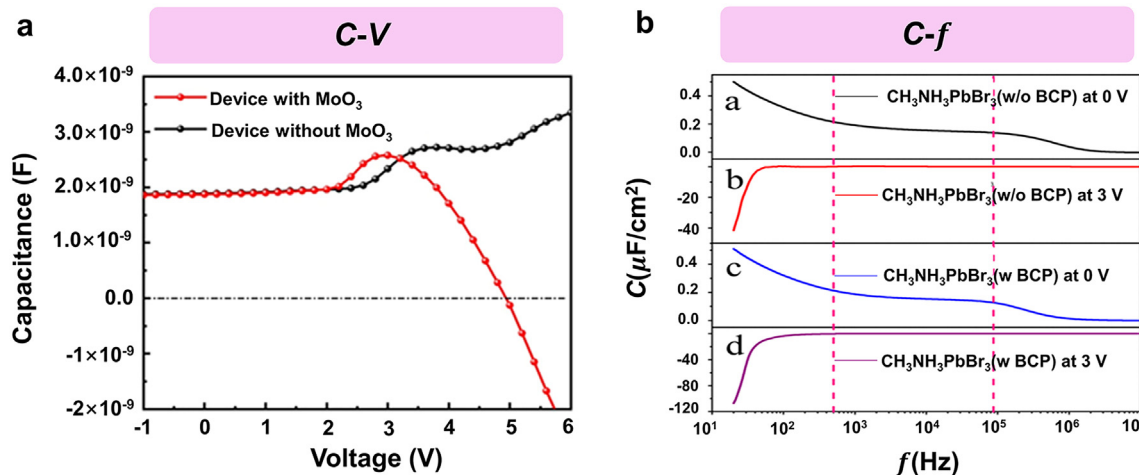


**FIG. 13.** (a) C–V curve with or without  $\text{MoO}_3$ . Reproduced with permission from Choy *et al.*, Commun. Mater. 1, 1 (2020). Copyright 2020 Nature Publishing Group.<sup>141</sup> (b) C–f curve for PeLEDs with or without BCP at dc bias voltage 0 and 3 V, respectively. Reproduced with permission from Hu *et al.*, ACS Appl. Energy Mater. 1, 6992 (2018). Copyright 2018 American Chemical Society.<sup>191</sup>

from Fig. 13(a), the flat part under the condition of DC-voltage less than 2 V is due to the existence of depletion region in PeLEDs, and the bias applied in this range cannot suppress the built-in voltage of PeLEDs. As the voltage increases from 2 V, the capacitance increases significantly, allowing charge injection and accumulation and gradually injected into the PeLED. Since electron injection remains unchanged, the rise can only be explained by hole injection enhancement. When the applied voltage is greater than 4 V, the black curve without  $\text{MoO}_3$  drops and then rises again, and conversely, the red curve with  $\text{MoO}_3$  keeps falling until the capacitance is negative, indicating that  $\text{MoO}_3$  is conducive to reducing  $w_0$  and thus achieving a more excellent e-h recombination.<sup>141</sup> Another way to verify the e-h radiative recombination for PeLEDs is to perform capacitance-frequency (C-f) measurements.<sup>195,196</sup> Figure 13(b) describes the C-f

spectra of PeLEDs with and without bathocuproine (BCP) modification at DC bias voltage 0 and 3 V. All C-f diagrams can be divided into three regions: I, II, and III. When no voltage is applied [(a) and (c) in Fig. 13(b)], the change of capacitance with BCP is similar to that of without BCP. When 3 V DC-voltage is applied [(b) and (d) in Fig. 13(b)], negative capacitance appears in the region I, representing the radiative recombination of electrons and holes. Moreover, by comparing b and d, PeLEDs containing BCP generate more negative capacitance, reflecting faster recombination, which is favorable for devices.<sup>191</sup>

#### 4. Simulation techniques

Simulation calculations can be introduced to verify experimental results during the characterization of the above charge carrier

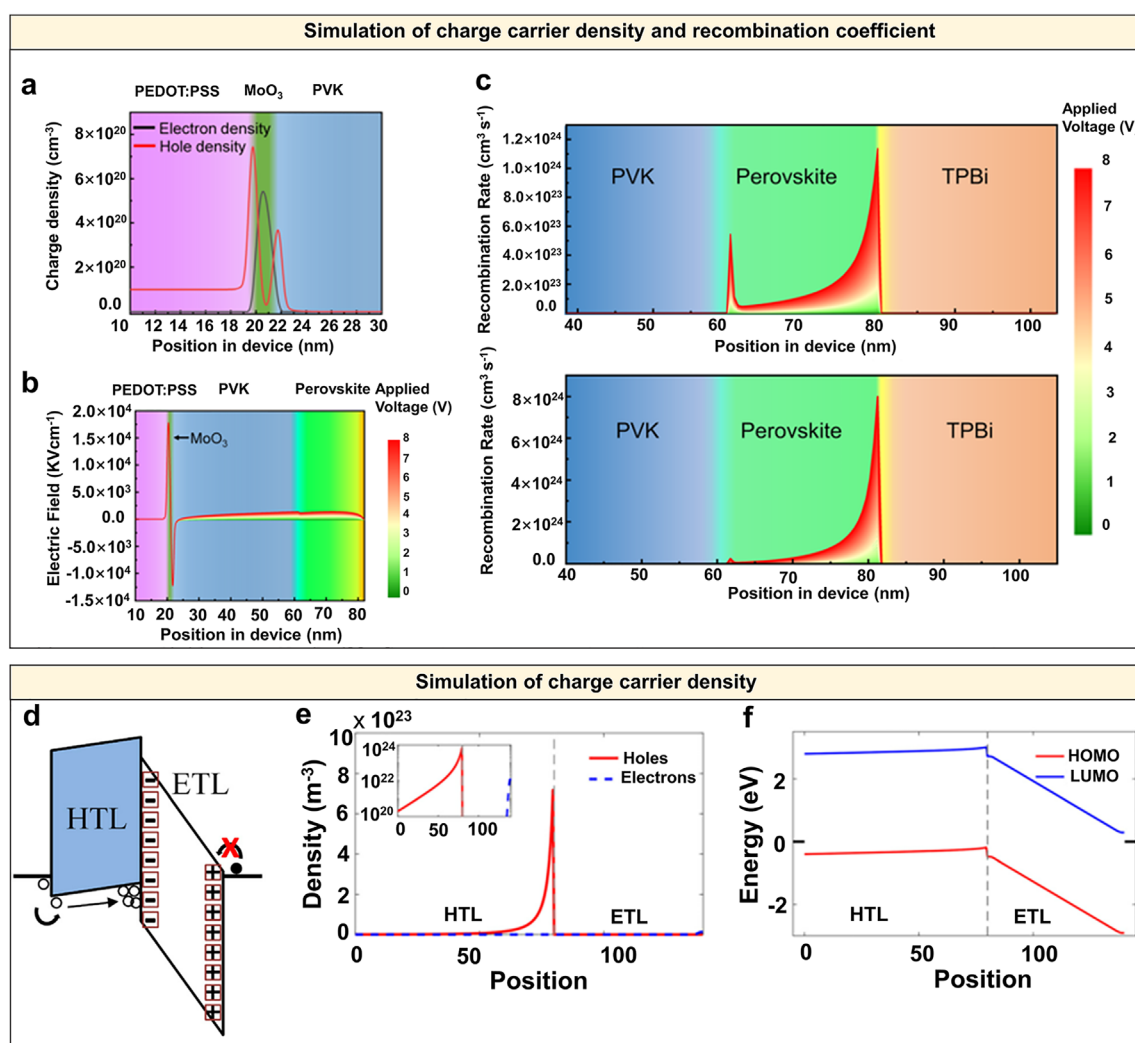


**FIG. 14.** (a) Charge-carrier density distribution in the device. (b) Electric field distribution in the device. (c) Distribution of recombination rate without (top) and with  $\text{MoO}_3$  (bottom). Reproduced with permission from Choy *et al.*, Commun. Mater. **1**, 1 (2020). Copyright 2020 Nature Publishing Group.<sup>141</sup> (d) Schematic diagram of the energy level of bilayer OLED. (e) The equilibrium charge-carrier densities of the hole (solid red lines) and electron (dashed blue lines) with offset voltage of 0 V are simulated using an 80-nm-thick HTL (left) and a 60-nm-thick ETL (right). The illustration shows a logarithmic representation. (f) Simulated energy level positions at 0 V. Reproduced with permission from Ruhstaller *et al.*, J. Appl. Phys. **121**, 175501 (2017). Copyright 2017 American Institute of Physics.<sup>197</sup>

dynamics, which is becoming a popular auxiliary characterization tool. For example, Fig. 13(a) has demonstrated by C-V technique that the addition of electric dipole  $\text{MoO}_3$  enhances the hole injection efficiency and promotes carrier injection balance. Simulation calculations of the carrier density distribution [Fig. 14(a)], electric field distribution [Fig. 14(b)] and recombination rate distribution [Fig. 14(c)] inside the device theoretically demonstrate the enhancement effect of  $\text{MoO}_3$  electric dipole layer on hole injection.<sup>141</sup> Figure 14(a) displays the carrier density distribution in PEDOT:PSS,  $\text{MoO}_3$ , and poly(9-vinylcarbazole) (PVK), finding that some electrons in PEDOT:PSS and PVK enter  $\text{MoO}_3$ , increasing the hole density in PEDOT:PSS and PVK around the  $\text{MoO}_3$  interface. The electric field distribution inside the device is shown in Fig. 14(b). There are two opposite electric fields, in which the positive electric field is conducive to the hole injection from PEDOT:PSS to PVK, while the negative electric field hinders the injection of electrons, achieving a better balance of carriers. The recombination rate distribution shows that the rate near the EML/TPBi [ $\text{TPBi} = 2,2',2''-(1,3,5\text{-Benzinetriyl})\text{-tris}(1\text{-phenyl-1-H-benzimidazole)}$ ] interface with  $\text{MoO}_3$  [Fig. 14(c), bottom] is seven times higher than that without  $\text{MoO}_3$  [Fig. 14(c), top]. The simulation calculations completely conform to the experimental results, as displayed in Fig. 13(a). In addition to simulating the carrier injection process, it is also possible to calculate the density of carriers. Züfle *et al.* selectively tested the charge-carrier density of the hole using the simulation method, as shown in Figs. 14(d)-14(f).<sup>197</sup> The energy level diagram in Fig. 14(d) shows that there is a large potential at ETL at 0 V, resulting in a negative electric field that hinders electron transport. Inversely, there is a positive electric field at the HTL, and holes can be injected into the HTL and accumulate at the interface of the HTL. The charge-carrier density is calculated as shown in Fig. 14(e). The maximum density of the hole is  $7 \times 10^{23} \text{ m}^{-3}$ , while the density of electrons is not tested. The simulated energy level diagram [Fig. 14(f)] also shows that holes have a driving force to inject into HTL, while electrons do not.

#### IV. CONCLUSION AND OUTLOOK

In this review, we summarize the charge-carrier dynamics process occurs especially in materials and devices in PeLEDs. For perovskite materials, the carrier dynamic processes are usually divided into bimolecular, monomolecular, and Auger recombination processes. The key factors limiting monomolecular and bimolecular radiative recombination are clarified by exploring the charge-carrier dynamics of perovskite materials. By passivating surface defects, such as metal cations or Lewis acids neutralize negative charge and anion or Lewis base neutralize positive charge, non-radiative recombination can be effectively suppressed, with the PLQY approaching 100%. Auger recombination can be effectively inhibited while maintaining the PLQY by reducing exciton binding energy and further passivation of defects. In addition to the above intrinsic recombination process, STEs luminescence has also been observed with the broad fluorescence spectrum and large Stokes shift. For low-dimensional and double perovskites, most of them show the recombination luminescence of STEs, which not only provides a new type of broad-spectrum emission material, but also provides a richer choice for white light emission of a single matrix.

In addition to perovskite materials, the study of interface dynamics in PeLEDs is equally important. A series of measures, such as interface engineering and energy level control, have been taken to improve the charge-carrier injection imbalance at interfaces, so as to enhance

the radiative recombination rate. For example, a double-layer HTL is introduced to reduce the hole injection barrier or an insulating layer between the ETL and the EML can inhibit the excess electron injection, which improves the charge-carrier balance in PeLEDs. Moreover, the Tr-EL, EI, TOF, TRPL, and other technologies can be used to directly observe the carrier mobility, density and lifetime, thus revealing the charge-carrier dynamics process in PeLEDs.

The rapid improvement of the efficiency of PeLEDs has been realized from perovskite composition, energy level regulation and interface engineering. However, some urgent problems should be given high attention: (i) At present, most reported passivation techniques for perovskite defects can reduce the non-radiative recombination and thus improve PLQY. Due to the variety and complexity of perovskite defects, it is necessary to select specific passivators. The negatively charged defects are neutralized mainly by metal or organic cations, or by Lewis acid coordination bonds. For positive charge defects, they can be neutralized by anions or Lewis bases. Although the passivation of perovskites has been studied a lot in this review, the specific passivation effect and internal passivation mechanism need to be further discussed. (ii) Although the PLQYs of perovskites are close to 100% using passivation defects, the carrier injection imbalance can cause the aggregation of electrons or holes in PeLEDs, resulting in non-radiative recombination, which greatly limits the device performance. A series of measures have been taken to improve the energy level and charge-carrier transport performance of each layer structure, thus improving charge-carrier injection balance. However, there is still a lot of work to be done in selecting both carrier mobility matching and energy level matching. In addition, the PN characteristics of perovskite materials will affect the holes or electrons injection capacity, which is also worth exploring. (iii) The process of carrier injection and recombination in PeLEDs are studied by means of Tr-EL, impedance analysis, and theoretical calculations. These technologies, which can more directly and intuitively observe the carrier transport operation, will become important tools for PeLEDs research.

#### ACKNOWLEDGMENTS

This work was financially supported by the Training Program of the Major Research Plan of the National Natural Science Foundation of China (No. 91964103), the Natural Science Foundation of Jiangsu Province (No. BK20180071), the National Natural Science Foundation of China (Nos. 52131304, 61725402, and 62004101), the Fundamental Research Funds for the Central Universities (Nos. 30919011109 and 30920041117), and the China Postdoctoral Science Foundation (No. 2020M681600).

#### AUTHOR DECLARATIONS

##### Conflict of Interest

The authors have no conflicts to disclose.

#### DATA AVAILABILITY

Data sharing is not applicable to this article as no new data were created or analyzed in this study.

#### REFERENCES

- <sup>1</sup>B. Chen, P. N. Rudd, S. Yang, Y. Yuan, and J. Huang, *Chem. Soc. Rev.* **48**(14), 3842 (2019).

- <sup>2</sup>Z. Chen, Z. Li, C. Zhang, X. F. Jiang, D. Chen, Q. Xue, M. Liu, S. Su, H. L. Yip, and Y. Cao, *Adv. Mater.* **30**(38), 1801370 (2018).
- <sup>3</sup>A. O. El-Ballouli, O. M. Bakr, and O. F. Mohammed, *J. Phys. Chem. Lett.* **11**(14), 5705 (2020).
- <sup>4</sup>J. Lim, M. T. Hörrantner, N. Sakai, J. M. Ball, S. Mahesh, N. K. Noel, Y.-H. Lin, J. B. Patel, D. P. McMeekin, M. B. Johnston, B. Wenger, and H. J. Snaith, *Energy Environ. Sci.* **12**(1), 169 (2019).
- <sup>5</sup>L. N. Quan, F. P. Garcia de Arquer, R. P. Sabatini, and E. H. Sargent, *Adv. Mater.* **30**(45), 1801996 (2018).
- <sup>6</sup>L. N. Quan, B. P. Rand, R. H. Friend, S. G. Mhaisalkar, T. W. Lee, and E. H. Sargent, *Chem. Rev.* **119**(12), 7444 (2019).
- <sup>7</sup>M. D. Smith, B. A. Connor, and H. I. Karunadasa, *Chem. Rev.* **119**(5), 3104 (2019).
- <sup>8</sup>S. D. Stranks and H. J. Snaith, *Nat. Nanotechnol.* **10**(5), 391 (2015).
- <sup>9</sup>Y. Zhou, J. Chen, O. M. Bakr, and H.-T. Sun, *Chem. Mater.* **30**(19), 6589 (2018).
- <sup>10</sup>M. Era, S. Morimoto, T. Tsutsui, and S. Saito, *Appl. Phys. Lett.* **65**(6), 676 (1994).
- <sup>11</sup>Z. K. Tan, R. S. Moghaddam, M. L. Lai, P. Docampo, R. Higler, F. Deschler, M. Price, A. Sadhanala, L. M. Pazos, D. Credgington, F. Hanusch, T. Bein, H. J. Snaith, and R. H. Friend, *Nat. Nanotechnol.* **9**(9), 687 (2014).
- <sup>12</sup>Y. Cao, N. Wang, H. Tian, J. Guo, Y. Wei, H. Chen, Y. Miao, W. Zou, K. Pan, Y. He, H. Cao, Y. Ke, M. Xu, Y. Wang, M. Yang, K. Du, Z. Fu, D. Kong, D. Dai, Y. Jin, G. Li, H. Li, Q. Peng, J. Wang, and W. Huang, *Nature* **562**(7726), 249 (2018).
- <sup>13</sup>T. Chiba, Y. Hayashi, H. Ebe, K. Hoshi, J. Sato, S. Sato, Y.-J. Pu, S. Ohisa, and J. Kido, *Nat. Photonics* **12**(11), 681 (2018).
- <sup>14</sup>K. Lin, J. Xing, L. N. Quan, F. P. G. de Arquer, X. Gong, J. Lu, L. Xie, W. Zhao, D. Zhang, C. Yan, W. Li, X. Liu, Y. Lu, J. Kirman, E. H. Sargent, Q. Xiong, and Z. Wei, *Nature* **562**(7726), 245 (2018).
- <sup>15</sup>W. Xu, Q. Hu, S. Bai, C. Bao, Y. Miao, Z. Yuan, T. Borzda, A. J. Barker, E. Tyukalova, Z. Hu, M. Kawecki, H. Wang, Z. Yan, X. Liu, X. Shi, K. Uvdal, M. Fahlman, W. Zhang, M. Duchamp, J.-M. Liu, A. Petrozza, J. Wang, L.-M. Liu, W. Huang, and F. Gao, *Nat. Photonics* **13**(6), 418 (2019).
- <sup>16</sup>B. Zhao, S. Bai, V. Kim, R. Lamboll, R. Shivanna, F. Auras, J. M. Richter, L. Yang, L. Dai, M. Alsari, X.-J. She, L. Liang, J. Zhang, S. Lilliu, P. Gao, H. J. Snaith, J. Wang, N. C. Greenham, R. H. Friend, and D. Di, *Nat. Photonics* **12**(12), 783 (2018).
- <sup>17</sup>J. Cui, Y. Liu, Y. Deng, C. Lin, Z. Fang, C. Xiang, P. Bai, K. Du, X. Zuo, K. Wen, S. Gong, H. He, Z. Ye, Y. Gao, H. Tian, B. Zhao, J. Wang, and Y. Jin, *Sci. Adv.* **7**(41), eabg8458 (2021).
- <sup>18</sup>X. Zheng, S. Yuan, J. Liu, J. Yin, F. Yuan, W.-S. Shen, K. Yao, M. Wei, C. Zhou, K. Song, B.-B. Zhang, Y. Lin, M. N. Hedhili, N. Wehbe, Y. Han, H.-T. Sun, Z.-H. Lu, T. D. Anthopoulos, O. F. Mohammed, E. H. Sargent, L.-S. Liao, and O. M. Bakr, *ACS Energy Lett.* **5**(3), 793 (2020).
- <sup>19</sup>S. O. Jeon, K. H. Lee, J. S. Kim, S.-G. Ihn, Y. S. Chung, J. W. Kim, H. Lee, S. Kim, H. Choi, and J. Y. Lee, *Nat. Photonics* **15**(3), 208 (2021).
- <sup>20</sup>R. Su, Y. Zhao, F. Yang, L. Duan, J. Lan, Z. Bin, and J. You, *Sci. Bull.* **66**(5), 441 (2021).
- <sup>21</sup>G. H. Ahmed, J. Yin, O. M. Bakr, and O. F. Mohammed, *ACS Energy Lett.* **6**(4), 1340 (2021).
- <sup>22</sup>E. S. Vasileiadou, B. Wang, I. Spanopoulos, I. Hadar, A. Navrotsky, and M. G. Kanatzidis, *J. Am. Chem. Soc.* **143**(6), 2523 (2021).
- <sup>23</sup>Y. Li, H. Wu, W. Qi, X. Zhou, J. Li, J. Cheng, Y. Zhao, Y. Li, and X. Zhang, *Nano Energy* **77**, 105237 (2020).
- <sup>24</sup>W. Cao, C. Xiang, Y. Yang, Q. Chen, L. Chen, X. Yan, and L. Qian, *Nat. Commun.* **9**(1), 2608 (2018).
- <sup>25</sup>Y. Jiang, X. Wang, and A. Pan, *Adv. Mater.* **31**(47), 1806671 (2019).
- <sup>26</sup>K. Galkowski, A. Mitioglu, A. Miyata, P. Plochocka, O. Portugall, G. E. Eperon, J. T.-W. Wang, T. Stergiopoulos, S. D. Stranks, H. J. Snaith, and R. J. Nicholas, *Energy Environ. Sci.* **9**(3), 962 (2016).
- <sup>27</sup>M. Saba, F. Quochi, A. Mura, and G. Bongiovanni, *Acc. Chem. Res.* **49**(1), 166 (2016).
- <sup>28</sup>X. Chen, H. Lu, K. Wang, Y. Zhai, V. Lunin, P. C. Sercel, and M. C. Beard, *J. Am. Chem. Soc.* **143**(46), 19438 (2021).
- <sup>29</sup>K. Zheng, K. Žídek, M. Abdellah, J. Chen, P. Chábera, W. Zhang, M. J. Al-Marri, and T. Pullerits, *ACS Energy Lett.* **1**(6), 1154 (2016).
- <sup>30</sup>N. T. P. Hartono, S. Sun, M. C. Gélvez-Rueda, P. J. Pierone, M. P. Erodici, J. Yoo, F. Wei, M. Bawendi, F. C. Grozema, M.-J. Sher, T. Buonassisi, and J.-P. Correa-Baena, *J. Mater. Chem. A* **7**(41), 23949 (2019).
- <sup>31</sup>L. M. Herz, *Annu. Rev. Phys. Chem.* **67**, 65 (2016).
- <sup>32</sup>G. Xing, B. Wu, X. Wu, M. Li, B. Du, Q. Wei, J. Guo, E. K. Yeow, T. C. Sum, and W. Huang, *Nat. Commun.* **8**(1), 14558 (2017).
- <sup>33</sup>M. Gao, H. Liu, S. Yu, S. Louisia, Y. Zhang, D. P. Nenon, A. P. Alivisatos, and P. Yang, *J. Am. Chem. Soc.* **142**(19), 8871 (2020).
- <sup>34</sup>M. Ren, S. Cao, J. Zhao, B. Zou, and R. Zeng, *Nano-Micro Lett.* **13**(1), 163 (2021).
- <sup>35</sup>J. Shamsi, A. S. Urban, M. Imran, L. De Trizio, and L. Manna, *Chem. Rev.* **119**(5), 3296 (2019).
- <sup>36</sup>X. K. Liu, W. Xu, S. Bai, Y. Jin, J. Wang, R. H. Friend, and F. Gao, *Nat. Mater.* **20**(1), 10 (2021).
- <sup>37</sup>J. S. Manser and P. V. Kamat, *Nat. Photonics* **8**(9), 737 (2014).
- <sup>38</sup>X. Zhang, J. X. Shen, and C. G. Van de Walle, *Adv. Energy Mater.* **10**(13), 1902830 (2019).
- <sup>39</sup>Q. Wei, X. Li, C. Liang, Z. Zhang, J. Guo, G. Hong, G. Xing, and W. Huang, *Adv. Opt. Mater.* **7**(17), 1900080 (2019).
- <sup>40</sup>C. Zou, Y. Liu, D. S. Ginger, and L. Y. Lin, *ACS Nano* **14**(5), 6076 (2020).
- <sup>41</sup>H. C. Cho, S. H. Jeong, M. H. Park, Y. H. Kim, C. Wolf, C. L. Lee, J. H. Heo, A. Sadhanala, N. Myoung, S. Yoo, S. H. Im, R. H. Friend, and T. W. Lee, *Science* **350**(6265), 1222 (2015).
- <sup>42</sup>Z. Xiao, R. A. Kerner, L. Zhao, N. L. Tran, K. M. Lee, T.-W. Koh, G. D. Scholes, and B. P. Rand, *Nat. Photonics* **11**(2), 108 (2017).
- <sup>43</sup>P. Du, J. Li, L. Wang, L. Sun, X. Wang, X. Xu, L. Yang, J. Pang, W. Liang, J. Luo, Y. Ma, and J. Tang, *Nat. Commun.* **12**(1), 4751 (2021).
- <sup>44</sup>S. Feldmann, S. Macpherson, S. P. Senanayak, M. Abdi-Jalebi, J. P. H. Rivett, G. Nan, G. D. Tainter, T. A. S. Doherty, K. Frohma, E. Ringe, R. H. Friend, H. Sirringhaus, M. Saliba, D. Beljonne, S. D. Stranks, and F. Deschler, *Nat. Photonics* **14**(2), 123 (2019).
- <sup>45</sup>R. Li, C. Yi, R. Ge, W. Zou, L. Cheng, N. Wang, J. Wang, and W. Huang, *Appl. Phys. Lett.* **109**(15), 151101 (2016).
- <sup>46</sup>Y. Jiang, J. Wei, and M. Yuan, *J. Phys. Chem. Lett.* **12**(10), 2593 (2021).
- <sup>47</sup>N. Wang, L. Cheng, R. Ge, S. Zhang, Y. Miao, W. Zou, C. Yi, Y. Sun, Y. Cao, R. Yang, Y. Wei, Q. Guo, Y. Ke, M. Yu, Y. Jin, Y. Liu, Q. Ding, D. Di, L. Yang, G. Xing, H. Tian, C. Jin, F. Gao, R. H. Friend, J. Wang, and W. Huang, *Nat. Photonics* **10**(11), 699 (2016).
- <sup>48</sup>L. Kong, X. Zhang, Y. Li, H. Wang, Y. Jiang, S. Wang, M. You, C. Zhang, T. Zhang, S. V. Kershaw, W. Zheng, Y. Yang, Q. Lin, M. Yuan, A. L. Rogach, and X. Yang, *Nat. Commun.* **12**(1), 1246 (2021).
- <sup>49</sup>C. Sun, Y. Jiang, M. Cui, L. Qiao, J. Wei, Y. Huang, L. Zhang, T. He, S. Li, H. Y. Hsu, C. Qin, R. Long, and M. Yuan, *Nat. Commun.* **12**(1), 2207 (2021).
- <sup>50</sup>Z. Yin, J. Leng, S. Wang, G. Liang, W. Tian, K. Wu, and S. Jin, *J. Am. Chem. Soc.* **143**(12), 4725 (2021).
- <sup>51</sup>S. Yuan, Z. K. Wang, L. X. Xiao, C. F. Zhang, S. Y. Yang, B. B. Chen, H. T. Ge, Q. S. Tian, Y. Jin, and L. S. Liao, *Adv. Mater.* **31**(44), 1904319 (2019).
- <sup>52</sup>L. Zhang, C. Sun, T. He, Y. Jiang, J. Wei, Y. Huang, and M. Yuan, *Light Sci. Appl.* **10**(1), 61 (2021).
- <sup>53</sup>C. Luo, C. Yan, W. Li, F. Chun, M. Xie, Z. Zhu, Y. Gao, B. Guo, and W. Yang, *Adv. Funct. Mater.* **30**(19), 2000026 (2020).
- <sup>54</sup>J. Song, J. Li, X. Li, L. Xu, Y. Dong, and H. Zeng, *Adv. Mater.* **27**(44), 7162 (2015).
- <sup>55</sup>G. Pan, X. Bai, W. Xu, X. Chen, Y. Zhai, J. Zhu, H. Shao, N. Ding, L. Xu, B. Dong, Y. Mao, and H. Song, *ACS Appl. Mater. Interfaces* **12**(12), 14195 (2020).
- <sup>56</sup>X. Shen, Y. Zhang, S. V. Kershaw, T. Li, C. Wang, X. Zhang, W. Wang, D. Li, Y. Wang, M. Lu, L. Zhang, C. Sun, D. Zhao, G. Qin, X. Bai, W. W. Yu, and A. L. Rogach, *Nano Lett.* **19**(3), 1552 (2019).
- <sup>57</sup>J. Zhang, L. Zhang, P. Cai, X. Xue, M. Wang, J. Zhang, and G. Tu, *Nano Energy* **62**, 434 (2019).
- <sup>58</sup>M. Liu, Q. Wan, H. Wang, F. Carulli, X. Sun, W. Zheng, L. Kong, Q. Zhang, C. Zhang, Q. Zhang, S. Brovelli, and L. Li, *Nat. Photonics* **15**(5), 379 (2021).
- <sup>59</sup>J. C. Blancon, H. Tsai, W. Nie, C. C. Stoumpos, L. Pedesseau, C. Katan, M. Kepenekian, C. M. M. Soe, K. Appavoo, M. Y. Sfeir, S. Tretiak, P. M. Ajayan, M. G. Kanatzidis, J. Even, J. J. Crochet, and A. D. Mohite, *Science* **355**, 1288 (2017).

- <sup>60</sup>Z. Yang, M. Wang, H. Qiu, X. Yao, X. Lao, S. Xu, Z. Lin, L. Sun, and J. Shao, *Adv. Funct. Mater.* **28**(14), 1705908 (2018).
- <sup>61</sup>N. Spitha, D. D. Kohler, M. P. Hautzinger, J. Li, S. Jin, and J. C. Wright, *J. Phys. Chem. C* **124**(31), 17430 (2020).
- <sup>62</sup>C. Wehrenfennig, G. E. Eperon, M. B. Johnston, H. J. Snaith, and L. M. Herz, *Adv. Mater.* **26**(10), 1584 (2014).
- <sup>63</sup>Y. Jiang, M. Cui, S. Li, C. Sun, Y. Huang, J. Wei, L. Zhang, M. Lv, C. Qin, Y. Liu, and M. Yuan, *Nat. Commun.* **12**(1), 336 (2021).
- <sup>64</sup>Y. Li, X. Luo, T. Ding, X. Lu, and K. Wu, *Angew. Chem. Int. Ed.* **59**, 14292 (2020).
- <sup>65</sup>S. A. March, D. B. Riley, C. Clegg, D. Webber, X. Liu, M. Dobrowolska, J. K. Furdyna, I. G. Hill, and K. C. Hall, *ACS Photonics* **4**(6), 1515 (2017).
- <sup>66</sup>M. H. Elkins, R. Pensack, A. H. Proppe, O. Voznyy, L. N. Quan, S. O. Kelley, E. H. Sargent, and G. D. Scholes, *J. Phys. Chem. Lett.* **8**(16), 3895 (2017).
- <sup>67</sup>J. Fu, Q. Xu, G. Han, B. Wu, C. H. A. Huan, M. L. Leek, and T. C. Sum, *Nat. Commun.* **8**(1), 1300 (2017).
- <sup>68</sup>S. D. Verma, Q. Gu, A. Sadhanala, V. Venugopalan, and A. Rao, *ACS Energy Lett.* **4**(3), 736 (2019).
- <sup>69</sup>B. Yang, J. Chen, S. Yang, F. Hong, L. Sun, P. Han, T. Pullerits, W. Deng, and K. Han, *Angew. Chem. Int. Ed. Engl.* **57**(19), 5359 (2018).
- <sup>70</sup>M. B. Price, J. Butkus, T. C. Jellicoe, A. Sadhanala, A. Briane, J. E. Halpert, K. Broch, J. M. Hodgkiss, R. H. Friend, and F. Deschler, *Nat. Commun.* **6**(1), 8420 (2015).
- <sup>71</sup>J. Yang, X. Wen, H. Xia, R. Sheng, Q. Ma, J. Kim, P. Tapping, T. Harada, T. W. Kee, F. Huang, Y. B. Cheng, M. Green, A. Ho-Baillie, S. Huang, S. Shrestha, R. Patterson, and G. Conibeer, *Nat. Commun.* **8**(1), 14120 (2017).
- <sup>72</sup>Y. Yang, D. P. Ostrowski, R. M. France, K. Zhu, J. van de Lagemaat, J. M. Luther, and M. C. Beard, *Nat. Photonics* **10**(1), 53 (2015).
- <sup>73</sup>W. J. Yin, T. Shi, and Y. Yan, *Adv. Mater.* **26**(27), 4653 (2014).
- <sup>74</sup>D. Luo, R. Su, W. Zhang, Q. Gong, and R. Zhu, *Nat. Rev. Mater.* **5**(1), 44 (2019).
- <sup>75</sup>M. Abdi-Jalebi, Z. Andaj-Garmaroudi, S. Cacovich, C. Stavrakas, B. Philippe, J. M. Richter, M. Alsari, E. P. Booker, E. M. Hutter, A. J. Pearson, S. Lilliu, T. J. Savenije, H. Rensmo, G. Divitini, C. Ducati, R. H. Friend, and S. D. Stranks, *Nature* **555**(7697), 497 (2018).
- <sup>76</sup>M. Abdi-Jalebi, M. Pazoki, B. Philippe, M. I. Dar, M. Alsari, A. Sadhanala, G. Divitini, R. Imani, S. Lilliu, J. Kullgren, H. Rensmo, M. Gratzel, and R. H. Friend, *ACS Nano* **12**(7), 7301 (2018).
- <sup>77</sup>J. Xu, A. Buin, A. H. Ip, W. Li, O. Voznyy, R. Comin, M. Yuan, S. Jeon, Z. Ning, J. J. McDowell, P. Kanjanaboons, J. P. Sun, X. Lan, L. N. Quan, D. H. Kim, I. G. Hill, P. Maksymovych, and E. H. Sargent, *Nat. Commun.* **6**(1), 7081 (2015).
- <sup>78</sup>Z. Yang, J. Dou, S. Kou, J. Dang, Y. Ji, G. Yang, W. Q. Wu, D. B. Kuang, and M. Wang, *Adv. Funct. Mater.* **30**(15), 1910710 (2020).
- <sup>79</sup>A. Abate, M. Saliba, D. J. Hollman, S. D. Stranks, K. Wojciechowski, R. Avolio, G. Grancini, A. Petrozza, and H. J. Snaith, *Nano Lett.* **14**(6), 3247 (2014).
- <sup>80</sup>N. Chen, T. Cai, W. Li, K. Hills-Kimball, H. Yang, M. Que, Y. Nagaoka, Z. Liu, D. Yang, A. Dong, C. Y. Xu, R. Zia, and O. Chen, *ACS Appl. Mater. Interfaces* **11**(18), 16855 (2019).
- <sup>81</sup>X. Gong, L. Guan, H. Pan, Q. Sun, X. Zhao, H. Li, H. Pan, Y. Shen, Y. Shao, L. Sun, Z. Cui, L. Ding, and M. Wang, *Adv. Funct. Mater.* **28**(50), 1804286 (2018).
- <sup>82</sup>J. Navas, A. Sanchez-Coronilla, J. J. Gallardo, N. C. Hernandez, J. C. Pinero, R. Alcantara, C. Fernandez-Lorenzo, D. M. De los Santos, T. Aguilar, and J. Martin-Calleja, *Nanoscale* **7**(14), 6216 (2015).
- <sup>83</sup>M. I. Saidaminov, J. Kim, A. Jain, R. Quintero-Bermudez, H. Tan, G. Long, F. Tan, A. Johnston, Y. Zhao, O. Voznyy, and E. H. Sargent, *Nat. Energy* **3**(8), 648 (2018).
- <sup>84</sup>R. Begum, M. R. Parida, A. L. Abdelhady, B. Murali, N. M. Alyami, G. H. Ahmed, M. N. Hedhili, O. M. Bakr, and O. F. Mohammed, *J. Am. Chem. Soc.* **139**(2), 731 (2017).
- <sup>85</sup>K. Kobayashi, H. Hasegawa, Y. Takahashi, J. Harada, and T. Inabe, *Mater. Chem. Front.* **2**(7), 1291 (2018).
- <sup>86</sup>T. Oku, Y. Ohishi, and A. Suzuki, *Chem. Lett.* **45**(2), 134 (2016).
- <sup>87</sup>J. T.-W. Wang, Z. Wang, S. Pathak, W. Zhang, D. W. deQuilettes, F. Wisnivesky-Rocca-Rivarola, J. Huang, P. K. Nayak, J. B. Patel, H. A. Mohd Yusof, Y. Vaynzof, R. Zhu, I. Ramirez, J. Zhang, C. Ducati, C. Grovenor, M. B. Johnston, D. S. Ginger, R. J. Nicholas, and H. J. Snaith, *Energy Environ. Sci.* **9**(9), 2892 (2016).
- <sup>88</sup>Q. Jiang, Y. Zhao, X. Zhang, X. Yang, Y. Chen, Z. Chu, Q. Ye, X. Li, Z. Yin, and J. You, *Nat. Photonics* **13**(7), 460 (2019).
- <sup>89</sup>W. Chen, Y. Wang, G. Pang, C. W. Koh, A. B. Djurišić, Y. Wu, B. Tu, F. Z. Liu, R. Chen, H. Y. Woo, X. Guo, and Z. He, *Adv. Funct. Mater.* **29**(27), 1808855 (2019).
- <sup>90</sup>S. Lee, J. H. Park, B. R. Lee, E. D. Jung, J. C. Yu, D. Di Nuzzo, R. H. Friend, and M. H. Song, *J. Phys. Chem. Lett.* **8**(8), 1784 (2017).
- <sup>91</sup>R. Wang, J. Xue, K.-L. Wang, Z.-K. Wang, Y. Luo, D. Fenning, G. Xu, S. Nuryyeva, T. Huang, Y. Zhao, J. L. Yang, J. Zhu, M. Wang, S. Tan, I. Yavuz, K. N. Houk, and Y. Yang, *Science* **366**(6472), 1509 (2019).
- <sup>92</sup>L. Si, S. Tao, Y. Chen, X. Niu, C. K. Onwudinanti, C. Hu, Z. Qiu, Z. Xu, G. Zheng, L. Wang, Y. Zhang, L. Li, H. Liu, Y. Lun, J. Hong, X. Wang, Y. Liu, H. Xie, Y. Gao, Y. Bai, S. Yang, G. Brocks, Q. Chen, and H. Zhou, *Nat. Energy* **4**(5), 408 (2019).
- <sup>93</sup>L. N. Quan, D. Ma, Y. Zhao, O. Voznyy, H. Yuan, E. Bladt, J. Pan, F. P. Garcia de Arquer, R. Sabatini, Z. Piontowski, A. H. Emwas, P. Todorovic, R. Quintero-Bermudez, G. Walters, J. Z. Fan, M. Liu, H. Tan, M. I. Saidaminov, L. Gao, Y. Li, D. H. Anjum, N. Wei, J. Tang, D. W. McCamant, M. B. J. Roeffaers, S. Bals, J. Hofkens, O. M. Bakr, Z. H. Lu, and E. H. Sargent, *Nat. Commun.* **11**(1), 170 (2020).
- <sup>94</sup>Z. Fang, W. Chen, Y. Shi, J. Zhao, S. Chu, J. Zhang, and Z. Xiao, *Adv. Funct. Mater.* **30**(12), 1909754 (2020).
- <sup>95</sup>J. Li, L. Xu, T. Wang, J. Song, J. Chen, J. Xue, Y. Dong, B. Cai, Q. Shan, B. Han, and H. Zeng, *Adv. Mater.* **29**(5), 1603885 (2017).
- <sup>96</sup>Y. Zhou, T. Fang, G. Liu, H. Xiang, L. Yang, Y. Li, R. Wang, D. Yan, Y. Dong, B. Cai, and H. Zeng, *Adv. Funct. Mater.* **31**(51), 2106871 (2021).
- <sup>97</sup>C. Bi, Z. Yao, X. Sun, X. Wei, J. Wang, and J. Tian, *Adv. Mater.* **33**(15), 2006722 (2021).
- <sup>98</sup>C. Zhang, S. Wang, X. Li, M. Yuan, L. Turynska, and X. Yang, *Adv. Funct. Mater.* **30**(31), 1910582 (2020).
- <sup>99</sup>Z. Liu, W. Qiu, X. Peng, G. Sun, X. Liu, D. Liu, Z. Li, F. He, C. Shen, Q. Gu, F. Ma, H. L. Yip, L. Hou, Z. Qi, and S. J. Su, *Adv. Mater.* **33**(43), 2103268 (2021).
- <sup>100</sup>Q. Zheng, W. Chu, C. Zhao, L. Zhang, H. Guo, Y. Wang, X. Jiang, and J. Zhao, *WIREs Comput. Mol. Sci.* **9**(6), e1411 (2019).
- <sup>101</sup>W. Chu, Q. Zheng, O. V. Prezhdo, J. Zhao, and W. A. Saidi, *Sci. Adv.* **6**(7), eaaw7453 (2020).
- <sup>102</sup>S. Kahmann, E. K. Tekelenburg, H. Duim, M. E. Kamminga, and M. A. Loi, *Nat. Commun.* **11**(1), 2344 (2020).
- <sup>103</sup>X. Y. Zhu and V. Podzorov, *J. Phys. Chem. Lett.* **6**(23), 4758 (2015).
- <sup>104</sup>M. Liang, W. Lin, Q. Zhao, X. Zou, Z. Lan, J. Meng, Q. Shi, I. E. Castelli, S. E. Canton, T. Pullerits, and K. Zheng, *J. Phys. Chem. Lett.* **12**(20), 4965 (2021).
- <sup>105</sup>M. D. Smith and H. I. Karunadasa, *Acc. Chem. Res.* **51**(3), 619 (2018).
- <sup>106</sup>S. A. Bretschneider, I. Ivanov, H. I. Wang, K. Miyata, X. Zhu, and M. Bonn, *Adv. Mater.* **30**(29), 1707312 (2018).
- <sup>107</sup>H. Liu, P. Lazzaroni, and C. Di Valentin, *Nanomaterials (Basel)* **8**(7), 481 (2018).
- <sup>108</sup>H. Xiang, J. Chen, R. Wang, and H. Zeng, *Appl. Phys. Lett.* **119**(8), 080502 (2021).
- <sup>109</sup>H. Xiang, C. Zuo, H. Zeng, and L. Ding, *J. Semicond.* **42**(3), 030202 (2021).
- <sup>110</sup>H. Xiang, R. Wang, J. Chen, F. Li, and H. Zeng, *Light Sci. Appl.* **10**(1), 206 (2021).
- <sup>111</sup>E. R. Dohner, E. T. Hoke, and H. I. Karunadasa, *J. Am. Chem. Soc.* **136**(5), 1718 (2014).
- <sup>112</sup>J. Luo, X. Wang, S. Li, J. Liu, Y. Guo, G. Niu, L. Yao, Y. Fu, L. Gao, Q. Dong, C. Zhao, M. Leng, F. Ma, W. Liang, L. Wang, S. Jin, J. Han, L. Zhang, J. Etheridge, J. Wang, Y. Yan, E. H. Sargent, and J. Tang, *Nature* **563**(7732), 541 (2018).
- <sup>113</sup>E. R. Dohner, A. Jaffe, L. R. Bradshaw, and H. I. Karunadasa, *J. Am. Chem. Soc.* **136**(38), 13154 (2014).
- <sup>114</sup>H. Lin, C. Zhou, J. Neu, Y. Zhou, D. Han, S. Chen, M. Worku, M. Chaaban, S. Lee, E. Berkwits, T. Siegrist, M. H. Du, and B. Ma, *Adv. Opt. Mater.* **7**(6), 1801474 (2019).

- <sup>115</sup>Z. Yuan, C. Zhou, Y. Tian, Y. Shu, J. Messier, J. C. Wang, L. J. van de Burgt, K. Kountouriotis, Y. Xin, E. Holt, K. Schanze, R. Clark, T. Siegrist, and B. Ma, *Nat. Commun.* **8**(1), 14051 (2017).
- <sup>116</sup>C. Zhou, H. Lin, H. Shi, Y. Tian, C. Pak, M. Shatruk, Y. Zhou, P. Djurovich, M. H. Du, and B. Ma, *Angew. Chem. Int. Ed. Engl.* **57**(4), 1021 (2018).
- <sup>117</sup>C. Zhou, H. Lin, M. Worku, J. Neu, Y. Zhou, Y. Tian, S. Lee, P. Djurovich, T. Siegrist, and B. Ma, *J. Am. Chem. Soc.* **140**(41), 13181 (2018).
- <sup>118</sup>J. Yu, J. Kong, W. Hao, X. Guo, H. He, W. R. Leow, Z. Liu, P. Cai, G. Qian, S. Li, X. Chen, and X. Chen, *Adv. Mater.* **31**(7), 1806385 (2019).
- <sup>119</sup>H. Hu, F. Meier, D. Zhao, Y. Abe, Y. Gao, B. Chen, T. Salim, E. E. M. Chia, X. Qiao, C. Deibel, and Y. M. Lam, *Adv. Mater.* **30**(36), 1707621 (2018).
- <sup>120</sup>J. Chen, J. Wang, X. Xu, J. Li, J. Song, S. Lan, S. Liu, B. Cai, B. Han, J. T. Precht, D. Ginger, and H. Zeng, *Nat. Photonics* **15**(3), 238 (2020).
- <sup>121</sup>R. Gautier, M. Paris, and F. Massuyeau, *J. Am. Chem. Soc.* **141**(32), 12619 (2019).
- <sup>122</sup>J. Bao and V. G. Hadjiev, *Nano-Micro Lett.* **11**(1), 26 (2019).
- <sup>123</sup>Z. Chu, Q. Ye, Y. Zhao, F. Ma, Z. Yin, X. Zhang, and J. You, *Adv. Mater.* **33**(18), 2007169 (2021).
- <sup>124</sup>J. Luo, L. Yang, Z. Tan, W. Xie, Q. Sun, J. Li, P. Du, Q. Xiao, L. Wang, X. Zhao, G. Niu, L. Gao, S. Jin, and J. Tang, *Adv. Mater.* **33**(38), 2101903 (2021).
- <sup>125</sup>Q. Wang, X. Wang, Z. Yang, N. Zhou, Y. Deng, J. Zhao, X. Xiao, P. Rudd, A. Moran, Y. Yan, and J. Huang, *Nat. Commun.* **10**(1), 5633 (2019).
- <sup>126</sup>F. Yan, J. Xing, G. Xing, L. Quan, S. T. Tan, J. Zhao, R. Su, L. Zhang, S. Chen, Y. Zhao, A. Huan, E. H. Sargent, Q. Xiong, and H. V. Demir, *Nano Lett.* **18**(5), 3157 (2018).
- <sup>127</sup>L. Yang, X. Li, Q. Yang, S. Wang, H. Tian, J. Ding, and L. Wang, *Adv. Funct. Mater.* **31**(6), 2007686 (2020).
- <sup>128</sup>J. Chen, H. Xiang, J. Wang, R. Wang, Y. Li, Q. Shan, X. Xu, Y. Dong, C. Wei, and H. Zeng, *ACS Nano* **15**(11), 17150 (2021).
- <sup>129</sup>A. Liu, C. Bi, R. Guo, M. Zhang, X. Qu, and J. Tian, *Adv. Opt. Mater.* **9**(18), 2002167 (2021).
- <sup>130</sup>Z. Wei and J. Xing, *J. Phys. Chem. Lett.* **10**(11), 3035 (2019).
- <sup>131</sup>X. Zhang, H. Lin, H. Huang, C. Reckmeier, Y. Zhang, W. C. Choy, and A. L. Rogach, *Nano Lett.* **16**(2), 1415 (2016).
- <sup>132</sup>X. Zhang, C. Sun, Y. Zhang, H. Wu, C. Ji, Y. Chuai, P. Wang, S. Wen, C. Zhang, and W. W. Yu, *J. Phys. Chem. Lett.* **7**(22), 4602 (2016).
- <sup>133</sup>C. H. Mak, X. Huang, R. Liu, Y. Tang, X. Han, L. Ji, X. Zou, G. Zou, and H.-Y. Hsu, *Nano Energy* **73**, 104752 (2020).
- <sup>134</sup>S. Baek, S. Kang, C. Son, S. J. Shin, J. H. Kim, J. Park, and S. W. Kim, *Adv. Opt. Mater.* **8**(8), 1901897 (2020).
- <sup>135</sup>M. Karlsson, Z. Yi, S. Reichert, X. Luo, W. Lin, Z. Zhang, C. Bao, R. Zhang, S. Bai, G. Zheng, P. Teng, L. Duan, Y. Lu, K. Zheng, T. Pullerits, C. Deibel, W. Xu, R. Friend, and F. Gao, *Nat. Commun.* **12**(1), 361 (2021).
- <sup>136</sup>C. Kuang, Z. Hu, Z. Yuan, K. Wen, J. Qing, L. Kobera, S. Abbrecht, J. Brus, C. Yin, H. Wang, W. Xu, J. Wang, S. Bai, and F. Gao, *Joule* **5**(3), 618 (2021).
- <sup>137</sup>J. Song, J. Li, L. Xu, J. Li, F. Zhang, B. Han, Q. Shan, and H. Zeng, *Adv. Mater.* **30**(30), 1800764 (2018).
- <sup>138</sup>X. Zhang, W. Yin, W. Zheng, and A. L. Rogach, *ACS Energy Lett.* **5**(9), 2927 (2020).
- <sup>139</sup>H. Cho, Y. H. Kim, C. Wolf, H. D. Lee, and T. W. Lee, *Adv. Mater.* **30**(42), 1704587 (2018).
- <sup>140</sup>Z. Ren, J. Yu, Z. Qin, J. Wang, J. Sun, C. C. S. Chan, S. Ding, K. Wang, R. Chen, K. S. Wong, X. Lu, W. J. Yin, and W. C. H. Choy, *Adv. Mater.* **33**(1), 2005570 (2021).
- <sup>141</sup>X. Xiao, K. Wang, T. Ye, R. Cai, Z. Ren, D. Wu, X. Qu, J. Sun, S. Ding, X. W. Sun, and W. C. H. Choy, *Commun. Mater.* **1**(1), 81 (2020).
- <sup>142</sup>Z. Chen, Z. Li, T. R. Hopper, A. A. Bakulin, and H. L. Yip, *Rep. Prog. Phys.* **84**(4), 046401 (2021).
- <sup>143</sup>J. Xing, Y. Zhao, M. Askerka, L. N. Quan, X. Gong, W. Zhao, J. Zhao, H. Tan, G. Long, L. Gao, Z. Yang, O. Voznyy, J. Tang, Z. H. Lu, Q. Xiong, and E. H. Sargent, *Nat. Commun.* **9**(1), 3541 (2018).
- <sup>144</sup>C. Mai, D. Yu, J. Li, G. Huang, H. Zheng, L. Mu, Y. Cun, J. Wang, G. Xie, J. Wang, J. Peng, and Y. Cao, *Adv. Opt. Mater.* **8**(11), 1902177 (2020).
- <sup>145</sup>Z. Wang, F. Yuan, W. Sun, H. Shi, T. Hayat, A. Alsaedi, L. Fan, and Z. A. Tan, *Adv. Opt. Mater.* **7**(24), 1901299 (2019).
- <sup>146</sup>P. Schulz, D. Cahen, and A. Kahn, *Chem. Rev.* **119**(5), 3349 (2019).
- <sup>147</sup>Y. H. Kim, H. Cho, J. H. Heo, T. S. Kim, N. Myoung, C. L. Lee, S. H. Im, and T. W. Lee, *Adv. Mater.* **27**(7), 1248 (2015).
- <sup>148</sup>L. Meng, E. P. Yao, Z. Hong, H. Chen, P. Sun, Z. Yang, G. Li, and Y. Yang, *Adv. Mater.* **29**(4), 1603826 (2017).
- <sup>149</sup>D. B. Kim, J. C. Yu, Y. S. Nam, D. W. Kim, E. D. Jung, S. Y. Lee, S. Lee, J. H. Park, A.-Y. Lee, B. R. Lee, D. D. Nuzzo, R. H. Friend, and M. H. Song, *J. Mater. Chem. C* **4**(35), 8161 (2016).
- <sup>150</sup>X. F. Peng, X. Y. Wu, X. X. Ji, J. Ren, Q. Wang, G. Q. Li, and X. H. Yang, *J. Phys. Chem. Lett.* **8**(19), 4691 (2017).
- <sup>151</sup>Y. Xiang, G. Xie, Q. Li, L. Xue, Q. Xu, J. Zhu, Y. Tang, S. Gong, X. Yin, and C. Yang, *ACS Appl. Mater. Interfaces* **11**(32), 29105 (2019).
- <sup>152</sup>Y. Dou, D. Wang, G. Li, Y. Liao, W. Sun, J. Wu, and Z. Lan, *ACS Appl. Mater. Interfaces* **11**(35), 32159 (2019).
- <sup>153</sup>K. Wang, C. Wu, Y. Hou, D. Yang, T. Ye, J. Yoon, M. Sanghadasa, and S. Priya, *Energy Environ. Sci.* **13**(10), 3412 (2020).
- <sup>154</sup>N. Wijeyesinghe, A. Regoutz, F. Eisner, T. Du, L. Tsetseris, Y.-H. Lin, H. Faber, P. Pattanasattayavong, J. Li, F. Yan, M. A. McLachlan, D. J. Payne, M. Heaney, and T. D. Anthopoulos, *Adv. Funct. Mater.* **27**(35), 1701818 (2017).
- <sup>155</sup>Y. Liu, T. Wu, Y. Liu, T. Song, and B. Sun, *APL Mater.* **7**(2), 021102 (2019).
- <sup>156</sup>M. K. Gangishetty, S. Hou, Q. Quan, and D. N. Congreve, *Adv. Mater.* **30**(20), 1706226 (2018).
- <sup>157</sup>E. P. Yao, Z. Yang, L. Meng, P. Sun, S. Dong, Y. Yang, and Y. Yang, *Adv. Mater.* **29**(23), 1606859 (2017).
- <sup>158</sup>S. Lee, D. B. Kim, I. Hamilton, M. Daboczi, Y. S. Nam, B. R. Lee, B. Zhao, C. H. Jang, R. H. Friend, J. S. Kim, and M. H. Song, *Adv. Sci. (Weinh)* **5**(11), 1801350 (2018).
- <sup>159</sup>J. Lin, X. Dai, X. Liang, D. Chen, X. Zheng, Y. Li, Y. Deng, H. Du, Y. Ye, D. Chen, C. Lin, L. Ma, Q. Bao, H. Zhang, L. Wang, X. Peng, and Y. Jin, *Adv. Funct. Mater.* **30**(5), 1907265 (2019).
- <sup>160</sup>S. Ding, W. Wang, X. Xiao, X. Qu, Z. Wu, B. Xu, S. Chen, K. Wang, and X. W. Sun, *AIP Adv.* **10**(6), 065308 (2020).
- <sup>161</sup>Y. Liu, J. Cui, K. Du, H. Tian, Z. He, Q. Zhou, Z. Yang, Y. Deng, D. Chen, X. Zuo, Y. Ren, L. Wang, H. Zhu, B. Zhao, D. Di, J. Wang, R. H. Friend, and Y. Jin, *Nat. Photonics* **13**(11), 760 (2019).
- <sup>162</sup>W. Wang, Z. Wu, T. Ye, S. Ding, K. Wang, Z. Peng, and X. W. Sun, *J. Mater. Chem. C* **9**(6), 2115 (2021).
- <sup>163</sup>L. Zhang, X. Yang, Q. Jiang, P. Wang, Z. Yin, X. Zhang, H. Tan, Y. M. Yang, M. Wei, B. R. Sutherland, E. H. Sargent, and J. You, *Nat. Commun.* **8**(1), 15640 (2017).
- <sup>164</sup>J. Wang, N. Wang, Y. Jin, J. Si, Z. K. Tan, H. Du, L. Cheng, X. Dai, S. Bai, H. He, Z. Ye, M. L. Lai, R. H. Friend, and W. Huang, *Adv. Mater.* **27**(14), 2311 (2015).
- <sup>165</sup>M. You, H. Wang, F. Cao, C. Zhang, T. Zhang, L. Kong, L. Wang, D. Zhao, J. Zhang, and X. Yang, *ACS Appl. Mater. Interfaces* **12**(38), 43018 (2020).
- <sup>166</sup>T. Fang, T. Wang, X. Li, Y. Dong, S. Bai, and J. Song, *Sci. Bull.* **66**(1), 36 (2021).
- <sup>167</sup>M. Xu, Q. Peng, W. Zou, L. Gu, L. Xu, L. Cheng, Y. He, M. Yang, N. Wang, W. Huang, and J. Wang, *Appl. Phys. Lett.* **115**(4), 041102 (2019).
- <sup>168</sup>E. A. Duijnsteet, J. M. Ball, V. M. Le Corre, L. J. A. Koster, H. J. Snaith, and J. Lim, *ACS Energy Lett.* **5**(2), 376 (2020).
- <sup>169</sup>Toprasertpong, N. Kasamatsu, H. Fujii, T. Kada, S. Asahi, Y. Wang, K. Watanabe, M. Sugiyama, T. Kita, and Y. Nakano, *Appl. Phys. Lett.* **107**(4), 043901 (2015).
- <sup>170</sup>D. Shi, V. Adinolfi, R. Comin, M. Yuan, E. Alarousu, A. Buin, Y. Chen, S. Hoogland, A. Rothenberger, K. Katsiev, Y. Losoviy, X. Zhang, P. A. Dowben, O. F. Mohammed, E. H. Sargent, and O. M. Bakr, *Science* **347**(6221), 519 (2015).
- <sup>171</sup>J. Peng, Y. Chen, K. Zheng, T. Pullerits, and Z. Liang, *Chem. Soc. Rev.* **46**(19), 5714 (2017).
- <sup>172</sup>D. H. Kim, J. Park, Z. Li, M. Yang, J. S. Park, I. J. Park, J. Y. Kim, J. J. Berry, G. Rumbles, and K. Zhu, *Adv. Mater.* **29**(23), 1606831 (2017).
- <sup>173</sup>J. G. Labram, N. R. Venkatesan, C. J. Takacs, H. A. Evans, E. E. Perry, F. Wudl, and M. L. Chabinyc, *J. Mater. Chem. C* **5**(24), 5930 (2017).
- <sup>174</sup>O. E. Semonin, G. A. Elbaz, D. B. Straus, T. D. Hull, D. W. Paley, A. M. van der Zande, J. C. Hone, I. Kymissis, C. R. Kagan, X. Roy, and J. S. Owen, *J. Phys. Chem. Lett.* **7**(17), 3510 (2016).
- <sup>175</sup>H. Zhang, E. Debroye, W. Zheng, S. Fu, L. D. Virgilio, P. Kumar, M. Bonn, and H. I. Wang, *Sci. Adv.* **7**(52), eabj9066 (2021).
- <sup>176</sup>C. Wehrenfennig, M. Liu, H. J. Snaith, M. B. Johnston, and L. M. Herz, *Energy Environ. Sci.* **7**(7), 2269 (2014).

- <sup>177</sup>T. Niu, W. Zhu, Y. Zhang, Q. Xue, X. Jiao, Z. Wang, Y.-M. Xie, P. Li, R. Chen, F. Huang, Y. Li, H.-L. Yip, and Y. Cao, *Joule* **5**(1), 249 (2021).
- <sup>178</sup>B. Maynard, Q. Long, E. A. Schiff, M. Yang, K. Zhu, R. Kottokkaran, H. Abbas, and V. L. Dalal, *Appl. Phys. Lett.* **108**(17), 173505 (2016).
- <sup>179</sup>Q. Dong, Y. Fang, Y. Shao, P. Mulligan, J. Qiu, L. Cao, and J. Huang, *Science* **347**(6225), 967 (2015).
- <sup>180</sup>E. M. Hutter, G. E. Eperon, S. D. Stranks, and T. J. Savenije, *J. Phys. Chem. Lett.* **6**(15), 3082 (2015).
- <sup>181</sup>M.-J. Sher, C. B. Simmons, J. J. Krich, A. J. Akey, M. T. Winkler, D. Recht, T. Buonassisi, M. J. Aziz, and A. M. Lindenberg, *Appl. Phys. Lett.* **105**(5), 053905 (2014).
- <sup>182</sup>M. P. Erodici, P. J. Pierone, N. T. P. Hartono, J. Hidalgo, B. Lai, T. Buonassisi, J.-P. Correa-Baena, and M.-J. Sher, *Appl. Phys. Lett.* **118**(6), 063901 (2021).
- <sup>183</sup>M. Bag, L. A. Renna, R. Y. Adhikari, S. Karak, F. Liu, P. M. Lahti, T. P. Russell, M. T. Tuominen, and D. Venkataraman, *J. Am. Chem. Soc.* **137**(40), 13130 (2015).
- <sup>184</sup>G. Niu, W. Li, F. Meng, L. Wang, H. Dong, and Y. Qiu, *J. Mater. Chem. A* **2**(3), 705 (2014).
- <sup>185</sup>B. T. Diroll, S. Saha, V. M. Shalaev, A. Boltasseva, and R. D. Schaller, *Adv. Opt. Mater.* **8**(19), 2000652 (2020).
- <sup>186</sup>S. A. Sorenson, J. G. Patrow, and J. M. Dawlaty, *J. Phys. Chem. C* **120**(14), 7736 (2016).
- <sup>187</sup>P. Zeng, Q. Zhang, Y. Zhang, B. Cai, G. Feng, Y. Wang, C. Zeng, W.-H. Zhang, and M. Liu, *Appl. Phys. Lett.* **119**(10), 101101 (2021).
- <sup>188</sup>L. Chen, Y. Y. Tan, Z. X. Chen, T. Wang, S. Hu, Z. A. Nan, L. Q. Xie, Y. Hui, J. X. Huang, C. Zhan, S. H. Wang, J. Z. Zhou, J. W. Yan, B. W. Mao, and Z. Q. Tian, *J. Am. Chem. Soc.* **141**(4), 1665 (2019).
- <sup>189</sup>C. Zhao, W. Tian, Q. Sun, Z. Yin, J. Leng, S. Wang, J. Liu, K. Wu, and S. Jin, *J. Am. Chem. Soc.* **142**(35), 15091 (2020).
- <sup>190</sup>V. H. Nguyen, T. K. A. Hoang, Y. Kurokawa, and N. Usami, *J. Mater. Chem. C* **8**(41), 14481 (2020).
- <sup>191</sup>X. Sun, C. Han, K. Wang, H. Yu, J. Li, K. Lu, J. Qin, H. Yang, L. Deng, F. Zhao, Q. Yang, and B. Hu, *ACS Appl. Energy Mater.* **1**(12), 6992 (2018).
- <sup>192</sup>I. Zarazua, J. Bisquert, and G. Garcia-Belmonte, *J. Phys. Chem. Lett.* **7**(3), 525 (2016).
- <sup>193</sup>Y. Yang, Y. Yan, M. Yang, S. Choi, K. Zhu, J. M. Luther, and M. C. Beard, *Nat. Commun.* **6**(1), 7961 (2015).
- <sup>194</sup>Z. Wu, P. Liu, X. Qu, J. Ma, W. Liu, B. Xu, K. Wang, and X. W. Sun, *Adv. Opt. Mater.* **9**(17), 2100389 (2021).
- <sup>195</sup>Q. Niu, N. I. Craciun, G. A. H. Wetzelaer, and P. W. M. Blom, *Phys. Rev. Lett.* **120**(11), 116602 (2018).
- <sup>196</sup>R. Kumar, J. Kumar, P. Srivastava, D. Moghe, D. Kabra, and M. Bag, *ACS Appl. Mater. Interfaces* **12**(30), 34265 (2020).
- <sup>197</sup>S. Zufle, S. Altazin, A. Hofmann, L. Jager, M. T. Neukom, T. D. Schmidt, W. Brutting, and B. Ruhstaller, *J. Appl. Phys.* **121**(17), 175501 (2017).